Request for Funds for Construction of the BES MDC-III Detector

Submitted Jointly by Colorado State University
and the University of Hawaii on Behalf of the BES Collaboration

8 December 1997

Abstract

The BEPC e^+e^- storage ring and the BES detector have made important contributions to our understanding of the τ-lepton and charmed quark systems. The luminosity of BEPC has been improved and the capabilities of BES upgraded: they are uniquely positioned to make important measurements of the cross section for $e^+e^- \rightarrow$ *hadrons* as well as further studies of charmed particles. However, the BES Main Drift Chamber has developed a problem with prematurely aging feedthroughs. This aging produces high noise rates in the chamber, degrading tracking performance and compromising the event trigger. The most severe manifestation of feedthrough aging is the puncturing of the feedthrough wall. During the first few months of operation, 33 feedthroughs had either punctured or were drawing unacceptably high current, rendering 16% of the chamber unusable. The Main Drift Chamber is the most important component of the BES experiment. Without it, BES cannot operate, and because BES is the only colliding beam detector at IHEP, IHEP will effectively cease to function. This would have a uniquely severe impact since BES is the only high energy physics experiment in China. This proposal is for funds to build a new drift chamber. The new drift chamber will allow BES to take full advantage of other recently upgraded detector components and the upgraded performance of the BEPC collider. The total request for US funding is $624,375. Of this amount, the University of Hawaii is requesting $333,600 and Colorado State University is

requesting \$290,775. To meet the proposed Summer 1999 installation, we need to begin construction of the new chamber in early January 1998.

Contents

1 Introduction

The Beijing Spectrometer (BES) is a general purpose cylindrical detector built around the sole interaction point on the Beijing Electron Positron Collider (BEPC) at the Institute for High Energy Physics (IHEP) in Beijing, China. BEPC operates in an energy range that concentrates on tau and charm physics. Several US institutions joined the collaboration in 1991, after which BES made the most precise determination of the tau lepton mass. The US members participated in an upgrade of the BES detector, coincidental with an upgrade of BEPC. The upgrade was completed in early 1996.

The BES Main Drift Chamber (MDC-II) was built as part of the upgrade of the BES detector. The construction of the chamber was a joint effort involving both Chinese and American institutions. The endplates, outer cylinder, and feedthroughs were fabricated in the United States; the inner cylinder and electronics were produced in China. Wire and cables were procured by China, and personnel and space for construction were provided by China. Early in 1997 it became apparent that the high voltage feedthroughs in MDC-II were prematurely aging, causing unacceptable noise levels in the data and drawing large amounts of dark current. In some cases, feedthroughs would fail completely, loosing their ability to stand off high voltage. This last condition required turning off sections of the MDC-II.

A program to effect a temporary repair the MDC-II has been funded by DOE and undertaken. This repair involves lowering the voltage on damaged feedthroughs, while raising the voltage on so-far undamaged feedthroughs to maintain the electric field in the drift cells. Tests indicate, however, that the feedthroughs are continuing to deteriorate, leading to the inevitable death of the MDC-II. This proposal will detail the need to replace the MDC-II, and detail the justification and plan for the new Main Drift Chamber (MDC-III).

2 BES-II Physics

In its first five years of operation. the BES experiment accumulated event samples of 9 million J/ψ decays, 3.6 million $\psi(2S)$ decays, 25 pb^{-1} at the $\psi(4.03)$, and 5.0 pb^{-1} near $\tau^+\tau^-$ threshold. As part of the BES/BEPC upgrade, a number of changes to provide an order of magnitude improvement in the integrated luminosity per year are being implemented. These include:

- improved beampipe impedance;
- reduction in β_y^* from 8.5 cm to 5.0 cm;
- elimination of the second (unused) beam crossing; and
- the incorporation of beam emmittance control wigglers.

The first two of these have already been implemented and a factor of 1.5 improvement in the instantaneous luminosity has been demonstrated. This, together with improvements in the BEPC controls and the BES data acquisition system has resulted in a factor of two improvement in integrated luminosity per day.

With improved luminosity, it is reasonable to expect that in the three years following the completion of MDC-III, we can accumulate the following data samples:

- 100 pb^{-1} at the $\psi(3.77)$ for tagged D-meson studies;
- $\sim$ 50M J/ψ decays;
- $\sim$ 20M $\psi(2S)$ decays.

Subsequent to completing this, we can accumulate a comparable luminosity at higher energy, most likely near 4.13 GeV, for studies of tagged D_s decays. In addition, although we expect that a first scan of precision R measurements will be done prior to the implementation of MDC-III, it will likely be necessary to continue a program that follows up on these measurements.

In this section we outline some of the physics opportunities that data samples of these sizes could provide.

2.1 R Measurement

One of the primary goals of BES-II is to measure the ratio of the production cross-sections of hadrons to muons, commonly known as R:

$$R_{tot}(s) = \frac{\sigma_{tot}(e^+e^- \rightarrow hadrons)}{\sigma_{tot}(e^+e^- \rightarrow \mu^+\mu^-)}, \tag{1}$$

where $\sqrt{s}$ is the center-of-mass (CM) energy. The ratio R is extremely important to properly correct α(QED) at $q^2 = M_Z^2$, or $\alpha(M_Z^2)$, at the Z mass and the anomalous magnetic moment of the muon, a_μ. Precision tests of the Standard Model are now limited by the lack of precision on the ratio R which affects the corrections on $\alpha(M_Z^2)$. These corrections to $\alpha(M_Z^2)$ are most important in the tau-charm center of mass region where they are poorly known. R measurements are of fundamental importance and are uniquely available by the BES group.

This BES measurements will be done at distributed CM energies, producing an R measurement energy scan. The uncertainty on R in the BEPC energy range is currently 15-20%. By collecting 1000 hadronic events at each energy scan point, we expect to reduce the statistical error on R to less than 4% and the total error to 5-8%. This will be a significant improvement over previous measurements.

In the following sections, we discuss the corrections to the effective fine structure constant at the Z mass $\alpha(M_Z^2)$, the anomalous magnetic moment of the muon, a_μ, and a possible strategy for the measurements.

2.1.1 Determination of $\alpha(M_Z^2)$

The running of the effective fine structure constant is expressed as

$$\alpha(q^2) = \frac{\alpha_0}{1 - \Delta\alpha(q^2)}, \tag{2}$$

where α_0 is the electromagnetic fine structure constant. The correction term $\Delta\alpha(q^2)$ can be expressed as [1]

$$\Delta\alpha(q^2) = \frac{\alpha_0}{3\pi} \mathrm{P} \int_{4m_e^2}^{\infty} ds \frac{q^2}{s(q^2 - s)} R_{tot}(s). \tag{3}$$

This correction term can be decomposed into contributions from the leptons, the five lightest quarks, and the top quark as [2]

$$\Delta\alpha(q^2) = \Delta\alpha_\ell(q^2) + \Delta\alpha_{had}^{(5)}(q^2) + \Delta\alpha_{top}(q^2). \tag{4}$$

The leptonic contribution can be expressed simply as

$$\Delta\alpha_\ell(q^2) = \frac{\alpha_0}{3\pi} \sum_\ell \left[-\frac{5}{3} + ln \frac{q^2}{m_\ell^2} \right] \tag{5}$$

and the top quark contribution is accurately calculable. The contribution from the remaining five quarks is contained in $\Delta\alpha^{(5)}_{had}(q^2)$, which has contributions from both the continuum hadronic cross section and the $J^P = 1^-$ resonances.

The hadronic term $\Delta\alpha^{(5)}_{had}(q^2)$ evaluated at the Z mass is calculable from the integral

$$\Delta\alpha^{(5)}_{had}(M_Z^2) = -\frac{\alpha M_Z^2}{3\pi}\mathrm{Re}\int_{4m_\pi^2}^{\infty} ds \frac{R(s)}{s(s - M_Z^2 - i\epsilon)} \tag{6}$$

that incorporates measurements of R at all energies above $s = 4m_\pi^2$. In evaluating the above integral, Swartz [3] decomposes the hadronic cross section into four parts,

$$R(s) = R_{cont}(s) + R_{\pi^+\pi^-}(s) + R_{K^+K^-}(s) + R_{res}(s). \tag{7}$$

$R_{cont}(s)$ is the continuum contribution, evaluated above $s = 1$ GeV^2; $R_{\pi^+\pi^-}(s)$ is the pion-pair contribution evaluated from $s = 4m_\pi^2$ to 4 Gev^2; $R_{K^+K^-}(s)$ is the kaon-pair contribution evaluated from $s = 4m_K^2$ to 3.24 Gev^2; and $R_{res}(s)$ is the contribution from the $\omega(782)$, $\phi(1020)$, ψ, and Υ resonances.

2.1.2 Precision of $\alpha^{-1}(M_Z^2)$

Using old R measurements, the errors in $\Delta\alpha(M_Z^2)$ have been estimated to be 0.00042[4], 0.0007[2], 0.0007[5] and 0.00046[3]. These can be converted into errors in $\alpha^{-1}(M_Z^2)$ of 0.06, 0.09, 0.09 and 0.06 respectively.

Hadronic data from e^+e^- annihilation in the 2.5 - 5 GeV cm energy range now contribute 11% to the value of $\Delta\alpha(M_Z^2)$, but contribute 31% to the uncertainty in $\Delta\alpha(M_Z^2)$. An analysis[6] of the uncertainty that each of these parts contributes to the uncertainty in $\Delta\alpha(M_Z^2)$ showed that more than half of the error was from the continuum term $R_{cont}(s)$ in the region $1 < \sqrt{s} < 5$ Gev. It has been estimated [3] that new measurements of R with a 5% uncertainty in the center of mass energy region from 2.6 to 3.65 GeV will reduce the uncertainty in the continuum contribution to $\Delta\alpha_{had}$ by a factor of two.

2.1.3 Standard Model Effects

The precision of the Standard Model[6] has reached a level such that with parameters G_F and m_Z, the accuracy on $\Delta\alpha\,(m_Z^2)$ has become very important. In particular, the value of $\Delta\alpha\,(m_Z^2)$ influences the electroweak corrections on the top mass, m_t, and the Higgs mass, m_H. The effects [7] due to a change in $\Delta\alpha\,(m_Z^2)$ can be estimated by using the S and T variables. The change in the S and T variables as a function of the top and Higgs masses are given as

$$\Delta S = -\frac{1}{3\pi}\ln\left(\frac{m_t}{m_t^{REF}}\right)+\frac{1}{6\pi}\ln\left(\frac{M_H}{M_H^{REF}}\right), \tag{8}$$

$$\Delta T = \frac{3}{16\pi c^2 s^2}\ln\left(\frac{m_t^2-(m_t^{REF})^2}{m_Z^2}\right)-\frac{3}{8\pi c^2}\ln\left(\frac{M_H}{M_H^{REF}}\right). \tag{9}$$

The shift in $\sin^2\theta_{eff}^{lept}$ is given[8] as,

$$s^2 - s_o^2 = \Delta s^2 = \frac{\alpha\,(m_Z^2)}{c^2-s^2}\left(\frac{1}{4}S - s^2c^2T\right)-\frac{c^2s^2}{c^2-s^2}\left(\frac{\delta\alpha\,(m_Z^2)}{\alpha\,(m_Z^2)}\right), \tag{10}$$

where $s^2=\sin^2\theta_W$, $c^2=\cos^2\theta_W$, and s_o^2= predicted value of the MSM using values for the top and Higgs masses of m_t^{REF} and M_H^{REF}.

2.1.3.1 Implications for the Effective Weak Mixing Angle

Using the above formulae we can estimate the effects on the effective weak mixing angle. The current value of $\alpha^{-1}(M_Z^2)$ is 128.89±0.09. Using the error of 0.09, in the above formula, and $s^2 = 0.232$ and $c^2 = 0.768$, leads to an error in the effective weak mixing angle, δs^2, of 0.00023. The current measured values for the effective weak mixing angle from LEP and SLD are 0.23196±0.00028 and 0.23055±0.00041 and the updated predictions of the Standard Model[9] are 0.2318 with an error of 0.0001 due to the top and Higgs mass uncertainties. Thus the uncertainty in $\Delta\alpha(M_Z^2)$ is the largest source of error in tests of the Standard Model. Clearly a measurement that could reduce these errors will be very important.

2.1.3.2 Implications for the Higgs Mass

To estimate the effects on the Higgs mass, we can rewrite Δs^2 as a function of M_H and $\delta\alpha$ assuming the top mass is fixed,

$$\Delta s^2 = \frac{\alpha\left(m_Z^2\right)}{c^2 - s^2}\left(\frac{1}{24\pi} + \frac{3s^2}{8\pi}\right)\ln\left(\frac{M_H}{M_H^{REF}}\right) - \frac{c^2 s^2}{c^2 - s^2}\left(\frac{\delta\alpha\left(m_Z^2\right)}{\alpha\left(m_Z^2\right)}\right) \tag{11}$$

Using values of $\alpha^{-1}(M_Z^2) = 128.90 \pm 0.09, (0.0007$ fractional error), $s^2 = 0.232$, $c^2 = 0.768$, we can estimate the change in the prediction in the Higgs mass if the value of $\alpha^{-1}(M_Z^2)$ changes by 0.09 (1 standard deviation). If we use the Particle Data Tables for the Standard Model estimate[10] of the Higgs mass of 300 GeV, then a shift of $\alpha^{-1}(M_Z^2)$ by $+0.09$ will change this Higgs mass estimate to 444 GeV (Figure 1). Hence, we find that the Higgs mass predictions from the one loop corrections to the Standard Model are very dependent on the uncertainty in $\Delta\alpha(M_Z^2)$.

2.1.4 Determination of a_μ

The BES R measurement will be an important contribution to the calculation of the hadronic contribution to the anomalous magnetic moment of the muon, a_μ. The Standard Model prediction for a_μ can be decomposed into QED, hadronic, and weak contributions as

$$a_\mu = a_\mu^{QED} + a_\mu^{had} + a_\mu^{weak}. \tag{12}$$

As with the calculation of $\Delta\alpha(M_Z^2)$, the uncertainty in the calculation of a_μ is dominated by the uncertainty in the hadronic contribution. This contribution can be calculated from the dispersion integral

$$a_\mu^{had} = \left(\frac{\alpha m_\mu}{3\pi}\right)^2 \int_{4m_\pi^2}^{\infty} \frac{ds}{s^2} K(s) R(s) \tag{13}$$

where the kernel $K(s)$ is given by

$$K(s) = \frac{3s}{m_\mu^2}\left\{x^2\left(1 - \frac{x^2}{2}\right) + \left(1 + x^2\right)^2\left(1 + \frac{1}{x^2}\right)\left[\ln(1+x) - x + \frac{x^2}{2}\right] + \frac{1+x}{1-x}x^2\ln x\right\} \tag{14}$$

with

$$x = \frac{1-\beta}{1+\beta}, \beta = \sqrt{1 - \frac{4m_\mu^2}{s}}. \tag{15}$$

It has been calculated that with 26 energy scan points with 1000 hadrons each BES will reduce the error on the contribution to a_μ^{had} in the energy range 2.6 - 3.1 GeV from 0.12 ppm to 0.03.[11] This will be very important for experiment E821 at BNL (the (g-2) experiment) since they expect to reach a statistical error of 0.15 ppm. The energy range 2.0 - 2.6 GeV will continue to be a major source of error in a_μ^{had}. In fact, it may be more important with respect to E821 for BES to measure R in the lower energy region first. Because of the long time required to tune BEPC at energies below 2.5 GeV, we plan to measure R from 2.5 - 5.0 GeV first, before addressing the region from 2.0 - 2.6 GeV.

2.1.5 R Scan Strategy

In the spring of 1998 BES will be given two months of BEPC running time for the R scan. (The remaining three months will be divided between accelerator studies and running for the Beijing Synchrotron Radiation Facility.) For the first two weeks of that period, we will run on the J/ψ for detector checkout and calibration. Following that, we will conduct the R scan with the goal of collecting 1000 hadronic events at each of 50 center-of-mass energy points between 3 and 5 GeV. This will allow us to achieve a 3% statistical error at each point. Our systematic error will be 5%.

During this period we will also do energy calibration runs at the J/ψ and $\psi(2S)$, as well as single-beam runs for the measurement of backgrounds. Because of the importance of separating the continuum contribution to the hadronic cross section from the resonance contribution, the scan points have been chosen to maximize our knowledge of the resonance lineshapes (Figure 2.)

During the next run (October 1998 - June 1999) we will ask for 2 - 3 months to complete the R scan in the 2 - 3 GeV region.

2.1.6 Summary of R measurements

- Errors in R in the tau charm region will be reduced from 15-20% to ~3% statistical and ~5% systematic errors.

- Errors on $\sin^2\theta_{eff}^{lept}$ from $\Delta\alpha(M_Z^2)$ will be reduced by up to a factor two.
- Errors on a_μ^{had} may be reduced from 0.12 ppm to 0.03 ppm by a E_{cm} = 2.0 - 2.6 GeV energy scan.

2.2 D^+, D^0 and D_s Charm Physics

The charm meson branching ratios are extremely important to normalize charm and beauty rates. Essentially all charm rates rely on the $D^0 \to K^-\pi^+$, $D^+ \to K^-\pi^+\pi^+$ and $D_s \to \phi\pi^+$ branching ratios. These branching ratios of the D^0, D^+, and D_s are ideally measured in e^-e^+ production at energies where they can be pair produced. In such reactions, the branching ratios can be measured in a model independent method by measuring inclusive branching ratios and comparing them to exclusive measurements where both of the pair produced mesons are reconstructed. In the Mark III experiment[12] the D^0 and D^+ branching ratios were studied using the mode $e^-e^+ \to \psi(3.77) \to D^-D^+, D^0\overline{D^0}$ and a limit for the $D_s \to \phi\pi^+$ branching ratio using the reaction, $e^-e^+ \to D_s^{*-}D_s^+$ at $\sqrt{s}$=4.13 GeV was obtained. In the BES experiment[13] a statistics limited $D_s \to \phi\pi^+$ branching ratio, based on two events, was obtained using the reaction $e^-e^+ \to D_s^-D_s^+$ at $\sqrt{s}$=4.03 GeV.

2.2.1 Current Charm Meson Branching Ratios

The most precise measurements[14] of these branching ratios listed in the Particle Data tables come from the CLEO experiment. The measurement of the $D^0 \to K^-\pi^+$ branching ratio by CLEO uses the reaction $D^* \to \pi^+D^0$ for a model independent method. The current $D^0 \to K^-\pi^+$ branching ratios are listed in Table 1.

However, unlike the direct D^0 measurements, the $D^+ \to K^-\pi^+\pi^+$ measurements are model dependent measurements. The CLEO $D^+ \to K^-\pi^+\pi^+$ measurement relies on a prediction of the $D^{*+} \to \pi^\circ D^+/\pi^+D^0$ ratio. The $D^+ \to K^-\pi^+\pi^+$ branching ratios are listed in Table 2.

CLEO has reported two $D_s \to \phi\pi^+$ measurements that assume the matrix elements for $D^+ \to K^*l\nu$ and $D_s \to \phi l\nu$ are the same. In the second case, the $B \to D^*D_s$ measurement, the ratio $D_s \to \phi\pi^+/D^0 \to K^-\pi^+$ is determined in a partial reconstruction with large systematic errors. The Mark

Table 1: Current $D^0 \to K^-\pi^+$ Branching Ratios

Group	Method	Int. Luminosity	BR
Mark III	$e^-e^+ \to D^0\overline{D}^0$	9.3 pb^{-1} at 3.77 GeV	0.042±0.004 ± 0.004
CLEO	$D^* \to \pi^+ D^0$	1.8 fb^{-1}	0.0391±0.0008 ± 0.0017

Table 2: Current $D^+ \to K^-\pi^+\pi^+$ Branching Ratios

Group	Method	Int. Luminosity	BR
Mark III	$e^-e^+ \to D^+D^-$	9.3 pb^{-1} at 3.77 GeV	0.091±0.013 ± 0.004
CLEO	compare to $D^0 \to K^-\pi^+$	1.8 fb^{-1}	0.093±0.006 ± 0.008

III measurement is an upper limit and the BES measurement is based on only two events. The $D_s \to \phi\pi^+$ branching ratios are listed in Table 3.

Table 3: Current $D_s \to \phi\pi^+$ Branching Ratios

Group	Method	Int. Luminosity	BR
Mark III	$e^-e^+ \to D_s^{*+}D_s^-$	6.3 pb^{-1} at 4.13 GeV	< 0.041 at 90%CL
BES	$e^-e^+ \to D_s^+D_s^-$	23 pb^{-1} at 4.03 GeV	$0.039^{+0.051+0.018}_{-0.019-0.011}$
CLEO	$B \to D^* D_s$	2.5 fb^{-1}	0.0359±0.007 ± 0.0048
CLEO	$D_s \to \phi l\nu/\phi\pi^+$	1.7 fb^{-1}	0.051±0.004 ± 0.008

Due to the limited amount of data and the lack of precision, there is great interest to make model independent charm meson branching ratio measurements by the BES group.

2.2.2 Possible BES charm meson measurements

We have investigated what could be achieved with 100 pb^{-1} from the BES experiment running on the $\psi(3.77)$. This corresponds to a factor of 10 increase in statistics compared to the Mark III measurement. This should provide a factor of 3.3 statistical improvement over the old Mark III branching ratios. Hence, we would estimate the fractional statistical errors on the D^0 and the D^+ to be 2.9% and 4.3% respectively. These precisions are comparable to those from CLEO. As the pair production cross section of the charged and neutral D is $\sim$ 10 nb, an integrated luminosity of 100 pb^{-1} would produce 1M pairs of D's.

The D_s measurements have been very poor. The BES group attempted to measure this mode at $\sqrt{s} = 4.03$ GeV; however, the cross section ($\sigma B_{\phi\pi} = 11 \pm 2 \pm 2.5$ pb) was found to be more than a factor two smaller than that measured by the Mark III at $\sqrt{s} = 4.13$ GeV ($\sigma B_{\phi\pi} = 25 \pm 6$ pb). Hence, the proposal is to obtain 100 pb^{-1} at $\sqrt{s} = 4.13$ GeV. Given that BES obtained two events with 22 pb^{-1}, we would predict 16 events, to achieve a 25% fractional error on the $D_s \to \phi\pi^+$ branching ratio. In Table 4 we provide a summary of the precision that could be achieved by BES measurements.

Table 4: Projected BES Branching Ratios

Mode	Method	Int. Luminosity	Possible BR Errors
$D^0 \to K^-\pi^+$	$e^-e^+ \to D^0\overline{D}^0$	100 pb^{-1} at 3.77 GeV	0.04±0.0012
$D^+ \to K^-\pi^+\pi^+$	$e^-e^+ \to D^+D^-$	100 pb^{-1} at 3.77 GeV	0.09±0.0039
$D_s \to \phi\pi^+$	$e^-e^+ \to D_s^{*+}D_s^-$	100 pb^{-1} at 4.13 GeV	0.04±0.01

2.3 J/ψ Physics

2.3.1 Introduction

The J/ψ resonance is a bound state of charm and anti-charm quarks, whose mass lies below open charm threshold (twice the charm meson mass). The J/ψ decay follows the OZI rule and decays into light quarks. In a QCD picture, the pair of charm quarks annihilate into three gluons (hadronic) or into two gluons and a photon (radiative). Thus J/ψ radiative decays[15] provide a source of two gluons, where the gluons can form bound states or glueballs. Hence, J/ψ radiative decays are an ideal place to produce and to search for glueballs.

The recent calculations from Lattice QCD theorists predict masses of the scalar and tensor glueballs of ~1700 and ~2200 MeV. The results from the IBM and UK groups on the glueball masses are listed in Table 5.

Table 5: Lattice QCD predictions

Group	Scalar Mass (MeV)	Tensor Mass (MeV)
IBM	1740±41	2300
UKQCD	1572±65±55	2300

These calculations[16] use state of the art high speed computers. They predict masses and quantum numbers ($J^{PC} = 0^{++}, 2^{++}$) for glueballs[17] which are possible to be produced in J/ψ radiative decays. Conventional $q\overline{q}$ hadrons with similar masses and quantum numbers are abundantly produced and observed in J/ψ hadronic and radiative decays. If the glueballs exist in these mass ranges, they should be produced at some level in J/ψ radiative decays.

In addition it may be possible to produce hybrid states, $q\overline{q}$g, that are mixed states of a quark, anti-quark and a gluon[18]. It is possible that after the annihilation of the J/ψ into a photon and two gluons, one of the gluons changes into a $q\overline{q}$ pair, producing the right ingredients for a $q\overline{q}$g state. Hence, the J/ψ decays could be a source of hybrid states which could be investigated.

The old measurements[19] from Mark II, DM2, and Mark III, and recently from BES, have provided evidence for several new states, but require much higher statistics measurements to conclusively determine the spin-parity of these states. The primary scalar candidate is the $f_0(1710)$ and the tensor candidate is the $\xi(2.2)$. These states have been observed but the spin-parity results have not yet reached satisfactory results. Table 6 lists the PDG values for these measurements.

The above candidates certainly fit the predictions listed above, yet there

Table 6: Resonances in Radiative J/ψ decays (PDG values)

Resonance	mass (Mev)	width (MeV)
$f_J(1710)$	1697±4	175±9
$f_J(2220)$	2225±6	38^{+15}_{-13}

is no consensus that these are the glueballs due to the lack of high statistics data that can pin down the spin parity.

New and important results from the Crystal Barrel for a scalar resonance, the $f_0(1500)$ at 1500 MeV, and from the BNL experiment E852 for an exotic state ($J^{PC} = 1^{-+}$) at ∼1300 MeV have generated renewed interested in the search for non-$q\overline{q}$ states. There is great interest to search for these states in a high statistics data sample of J/ψ events.

The Mark III data sample was 5.8M and the recent BES data sample was ∼9.3M J/ψ events. An important increase should be at least a factor of five to achieve new and important physics. In the following sections, we briefly review the status of the tensor glueball candidate $\xi(2.2)$ and the scalar glueball candidate $f_J(1710)$ produced in J/ψ radiative decays, and the new states found from the Crystal Barrel and the E852 experiment. Then we consider the physics possibilities with a 50M J/ψ event sample.

In summary, the main points are:

- J/ψ radiative decays are an important place to search for glueball states.
- QCD Lattice Gauge Theories predict glueball states in the 1500-2500 MeV range.
- Previous measurements observe glueball candidates in J/ψ radiative decays which may be the glueballs predicted by Lattice Gauge theories, but the spin-parity information so far is incomplete.
- Recent measurements from other experiments observe new scalar and exotic states that could be candidates for glueballs and hybrids, and they may be produced in J/ψ decays.

- Only the BES experiment will have this important unique opportunity to study the above physics in the foreseeable future.

2.3.2 $\xi(2.2)$ Resonance

The $\xi(2.2)$ was seen originally by the Mark III group in K^+K^- and K_sK_s at a mass of 2.230 GeV, with no spin parity measurement. It was controversial due to the lack of evidence for the $\xi(2.2)$ from the DM2 group. Later the BES group observed the $\xi(2.2)$ at the same mass in the modes K^+K^- and K_sK_s. The width measurements of the $\xi(2.2)$ were usually limited by the detector mass resolutions. In addition, the BES group observed non-hidden strangeness modes of $\pi^+\pi^-$ and $p\overline{p}$. These new light quark modes are a very important aspect of $SU(3)$ singlet behaviour expected for a glueball candidate which should have both non-strange and hidden strangeness decay modes. The statistics, however, of these new published BES results are not very compelling and require improvement.

Recently the L3 group[20] observed evidence for the $\xi(2.2)$ in gluon jets of the three jet decay of the Z^0. They obtain a mass of 2.230$\pm$0.018 GeV with 51 events. They are not able to determine a width as it appears consistent with the detector mass resolution.

The next important step is to obtain the spin-parity of this state. This will require a subtantial increase in statistics. The distinction between spin 0 and spin 2 will require careful separation of the backgrounds from $J/\psi \rightarrow K^*K$ in the charged K^+K^- mode. The K_sK_s mode is cleaner since there is no background from $J/\psi \rightarrow \pi^0K_sK_s$ and the only limitation in the previous measurements were low statistics.

In summary, a data sample of 50M J/ψ events will improve the $\xi(2.2)$ in the following:

- Spin-parity test between spin 0 and spin 2.
- Increase statistics to confirm non-strange modes in $\pi^+\pi^-$ and $p\overline{p}$.
- Increase precision on the width measurement.

2.3.3 $f_J(1700)$ Resonance

The $\theta(1700)$ or $f_J(1710)$ resonance (as listed in the PGD) is a large signal observed in radiative J/ψ decays into K^+K^-, K_sK_s and $\pi^+\pi^-$. This state has been seen by Crystal Ball, Mark II, Mark III, DM2 and BES. It may also be the same state in the K^+K^- mode seen in central production by the WA76 group[21]. In addition to the evidence from radiative decays, this state is produced in the hadronic decay, $J/\psi \rightarrow \omega f_J(1710) \rightarrow \omega K\overline{K}$. This striking decay is OZI violating, but is expected if an $SU(3)$ singlet glueball is produced recoiling from non-strange quarks, but decaying into a final state with strange quarks.

The different experimental groups observe the same mass shape, but the spin-parity has been difficult due to overlapping states with different spin. A moment analysis that allows for overlapping scalar and tensor signals was made by the Mark III group[22]. They obtain clear evidence for a scalar signal in both $K\overline{K}$ and $\pi^+\pi^-$ over a tensor background (see Figure 3). A similar analysis was performed by the BES group (see Figure 4) which also observed a scalar signal but with slightly differing mass, width and branching fractions. These measurements are summarized in Table 7.

Table 7: Scalar Wave Spin Parity Results on the $f_J(1710)$

Group	Mass (MeV)	Width (MeV)	Branching Fraction ($\times 10^{-4}$)
Mark III	1704^{+16}_{-23}	124^{+52}_{-44}	$9.5^{+2.5}_{-2}$($K\overline{K}$ and $\pi\pi$)
BES	$1781 \pm 8^{+10}_{-31}$	$85 \pm 25^{+22}_{-19}$	$0.8 \pm 0.1^{+0.3}_{-0.1}$($K\overline{K}$)

In addition to measuring the spin-parity of this state, it will be very important to search for more decay modes. Possibly this state is being produced in $\pi^+\pi^+\pi^-\pi^-$ and $\pi^+\pi^-2\pi^0$ decays, as these radiative rates are six times the radiative rate of $f_J(1710)$ into $K\overline{K}$. If the $f_J(1710)$ behaves as an $SU(3)$ singlet, we should expect more non-strange final states, and it should be seen in multi-pion decay modes.

In summary, the $f_J(1710)$ study should include:

- Spin-parity test to distinguish between spin 0 and spin 2;
- Search for more $f_J(1710)$ decay modes, especially non-strange decay modes into 4π; and
- Search for production of the $f_J(1710)$ in hadronic decays.

2.3.4 Search for the $f_0(1500)$

The $f_0(1500)$ is a new scalar resonance observed by the Crystal Barrel group at LEAR[23] in $p\overline{p}$ collisions at rest. It decays into $\pi\pi$, $\eta\eta$, $\eta'\eta$ and $K\overline{K}$. There is confirming evidence of the $f_0(1500)$ from FNAL experiment E760 in a similar reaction, but they only observe it in a mass plot without spin-parity measurements. If the $f_0(1500)$ is a glueball, there probably should be evidence for this state in radiative J/ψ decays.

In the moment analysis[22] in $J/\psi \rightarrow \gamma\pi\pi$, $\gamma K\overline{K}$ from the Mark III experiment, no evidence for a scalar resonance at 1500 was seen. In an independent analysis[24] by D. Bugg of the Mark III data on $J/\psi \rightarrow \gamma\pi\pi\pi\pi$, compatible evidence was claimed for the $f_0(1500)$. In this analysis the two pion systems were assumed to be in a σ scalar resonance. However, the branching ratios of this analysis lead to predictions of a large signal in $J/\psi \rightarrow \gamma\pi\pi$ that is not observed[25].

With a high statistics J/ψ data sample, a search could be performed for radiative decays in the $\pi\pi$ and $\pi\pi\pi\pi$ modes. Given that this state is not copiously produced, at least according to the old Mark III and BES measurements, a tight upper limit may be possible in the $\pi\pi$ modes where the partial wave analysis is relatively simple. In the $\pi\pi\pi\pi$ mode, there is a very large and wide signal which could contain the $f_0(1500)$. A more comprehensive spin-parity analysis, previously attempted by D. Bugg, indicated that the inclusion of intermediate states, $\sigma\sigma$, $\rho\rho$ and $\pi\pi$ is necessary to understand the $\pi\pi\pi\pi$ mode. This analysis could be performed by the BES group with a large J/ψ sample.

2.3.5 Search for the $X(1300)$

The $X(1300)$ state is an exotic state decaying into $\eta\pi$ in a P wave for $J^{PC} = 1^{-+}$ near 1300 MeV. This state has been seen in $\eta\pi^+$ and $\eta\pi^o$ by GAMS, KEK-BENKEI and recently in a very high statistics study by the E852 at BNL. The BNL group[26] studied the reaction, $\pi^- p \rightarrow \eta\pi^- p$. In the p-wave channel they observe a phase shift compatible for a resonance with $J^{PC} = 1^{-+}$ which is an exotic spin-parity.

Such an exotic meson may be produced in either hadronic or radiative J/ψ decays. A possible place to search would be in the isospin conserving decays $J/\psi \rightarrow \omega\eta\pi\pi, \phi\eta\pi\pi$. Another place more suitable for producing the exotic quantum numbers would be in hadronic χ decays which have + parity and + charge conjugation. Such decay could be $\chi(1^{++}) \rightarrow X(1^{-+})\pi$, $X \rightarrow \eta\pi$ which is an s-wave production of the X and π. In this production there are no angular momentum barriers.

2.4 $\psi(2S)$ Physics

The BES experiment accumulated 3.6M $\psi(2S)$ events in two running periods corresponding to about five months of total running. With the increased luminosity of the the upgraded BEPC, it is reasonable to expect that we will be able to accumulate approximately 20M $\psi(2S)$ events in a dedicated running period of a few months. Such a sample of $\psi(2S)$ events will allow us to do measurements of unprecedented precision on properties of the charmonium system and decisive studies of the hadronic $\psi(2S)$ decays.

2.4.1 Charmonium physics

2.4.1.1 Search for the $\eta_c(2S)$

A major experimental issue for the charmonium particle system are the two charmonium states below open charm threshold that are still not well established: the $n = 2$ singlet S state, the $\eta_c(2S)$, and the $n = 1$ singlet P state, the $h_c(1P)$. The observation of these states and the determination of their mass would provide useful information on the spin-spin part of the charmonium potential.

The $\eta_c(2S)$ is expected to be produced in $\psi(2S)$ decays via the $M1$ radiative transition $\psi(2S) \rightarrow \gamma\eta_c(2S)$. Thus, with a sufficiently large $\psi(2S)$ data sample, the BES experiment could detect this process. (Transitions between the $\psi(2S)$ and the $h_c(1S)$ are forbidden and $\psi(2S)$ decays are not expected to be useful sources of this state.)

The Crystal Ball group [27] reported an excess of $E_\gamma \simeq 91$ MeV gamma rays from the inclusive $\psi(2S) \rightarrow \gamma X$ process, and interpret this as possible evidence for the $\eta_c(2S)$ with mass 3.594 ± 0.005 GeV. This result has not been confirmed by any other experiment.

Expectations for the mass of $\eta_c(2S)$:

The $\eta_c(2S)$ mass differs from that of the $\psi(2S)$ because of the hyperfine spin-spin interaction. In the simple potential model, the potential term for this splitting has the form [28]

$$\mathcal{H}_{hfs} = \frac{16\pi\alpha_s}{9m_c^2}\ \vec{S}_c \cdot \vec{S}_{\bar{c}}\ \delta^3(\vec{r}), \tag{16}$$

where m_c is the c-quark mass and $\vec{S}_c$ is its spin vector. This gives a simple relation for the ratio of $\psi(2S) - \eta_c(2S)$ and $J/\psi - \eta_c(1S)$ mass splitting:

$$\frac{\Delta M[\psi_{2S} - \eta_c(2S)]}{\Delta M[J/\psi - \eta_c(1S)]} \simeq \frac{\alpha_s(M_{\psi'})}{\alpha_s(M_{J/\psi})} \cdot \frac{|R_{2S}(0)|^2}{|R_{1S}(0)|^2}, \tag{17}$$

where the $R_{nS}(0)$ is the $c\bar{c}$ radial wavefunction at the origin. This can be evaluated from the ψ_{nS} leptonic width via the relation

$$\Gamma_{\psi_{nS}\to e^+e^-} = \frac{16\pi^2}{3}\alpha^2 e_c^2 \frac{|R_{nS}(0)|^2}{M_{\psi_{nS}}^2}, \tag{18}$$

leading to the relation

$$M_{\psi'} - M_{\eta_c'} \simeq \frac{\alpha_s(M_{\psi'})}{\alpha_s(M_{J/\psi})} \cdot \frac{M_{\psi'}^2}{M_{J/\psi}^2} \cdot \frac{\Gamma_{\psi'\to e^+e^-}}{\Gamma_{J/\psi\to e^+e^-}} \cdot (M_{J/\psi} - M_{\eta_c}). \tag{19}$$

Using the PDG values for the masses and widths, and $\alpha_s(M_{\psi'})/\alpha_s(M_{J/\psi}) = 0.9$, we find

$$M_{\psi'} - M_{\eta_c'} \simeq 65\text{MeV}; \quad \text{i.e.} \quad M_{\eta_c'} \simeq 3.62 \text{ GeV}. \tag{20}$$

This calculation ignores binding effects and treats the quarks as being on-shell. The authors of ref. [28] note that using $M_\psi/2$ instead of m_c in eqn. 16 may be a better way to account for binding effects. In this case, this cancels the $(M_{\psi'}/M_{J/\psi})^2$ factor on the right-hand side of eqn. 19, reducing the expected splitting to ~ 47 MeV and raising $M_{\eta_c'}$ to 3.64 GeV. These mass estimates are substantially above the Crystal Ball group's reported mass value.

The branching fraction $\mathcal{B}[\psi(2S) \to \gamma\eta_c(2S)]$:
The $\psi(2S) \to \gamma\eta_c(2S)$ process is an allowed $M1$ process with a width given by the relation [29]

$$\Gamma(\psi' \to \eta_c') = e_c^2\alpha(4k^3/3m_c^2)|I|^2(M_{\psi'}^2 + M_{\eta_c'}^2)/2M_{\psi'}^2, \tag{21}$$

where $e_c = 2/3$ is the c-quark charge, k is the photon momentum, and I is the initial-final state radial wavefunction overlap integral. With the exception of k, all of these factors are very nearly the same as for the $\psi(1S) \to \gamma\eta_c(1S)$ transition, leading to the relation:

$$\mathcal{B}[\psi(2S) \to \gamma\eta_c(2S)] = \frac{\Gamma[J/\psi \to \gamma\eta_c(1S)]}{\Gamma_{tot}(\psi_{2S})} \cdot \left(\frac{k_{\eta_c'}}{k_{\eta_c}}\right)^3 \simeq 2 \times 10^{-3}, \tag{22}$$

where the Crystal Ball value for the $\eta_c(2S)$ mass is used. For higher $\eta_c(2S)$ masses this reduces rapidly: for $M_{\eta_c'} = 3.62$GeV it decreases by a factor of three to $\mathcal{B} \simeq 7 \times 10^{-4}$; and for $M_{\eta_c'} = 3.64$GeV it decreases by a factor of eight to $\mathcal{B} \simeq 3 \times 10^{-4}$.

Expectations for $\eta_c(2S)$ decays:
Like the $\eta_c(1S)$, the $\eta_c(2S)$ decays are expected to be dominated by hadronic modes mediated by $c\bar{c}$ annihilation into two-gluon intermediate states. The total width can be estimated from the relation

$$\Gamma_{\eta_c'}^{tot} \simeq \frac{\alpha_s(M_{\eta_c'})^2}{\alpha_s(M_{\eta_c})^2} \cdot \frac{|R_{2S}(0)|^2}{|R_{1S}(0)|^2}\Gamma_{\eta_c}^{tot} = \frac{\alpha_s(M_{\psi'})^2}{\alpha_s(M_{J/\psi})^2} \cdot \frac{M_{\psi'}^2}{M_{J/\psi}^2} \cdot \frac{\Gamma_{\psi' \to e^+e^-}}{\Gamma_{J/\psi \to e^+e^-}} \cdot \Gamma_{\eta_c}^{tot} \simeq 8.1 \text{ MeV}. \tag{23}$$

This relatively large $\eta_c(2S)$ total width leads to the expectation that the relative rate for inter-charmonium transitions will be small. In this case, one expects that the branching fraction for $\eta_c(2S)$ to any specific hadronic final state will be the same as that for the corresponding $\eta_c(1S)$ decay [30].

$\eta_c(2S)$ search strategy:
In light of the above, a reasonable strategy for searching for the $\eta_c(2S)$ in the BES data is to concentrate on those decay modes that have been established for the $\eta_c(1S)$. In particular the $\psi(2S) \to \gamma$ + four charged particles final state is well suited for BES and covers many of the strategic decay modes.

Table 8: The expected numbers of detected events for $\psi(2S) \to \gamma\eta_c(2S)$, $\eta_c(2S) \to$ four charged particles.

$\eta_c(2S)$ decay final state	expected number of events $M_{\eta_c'}$(GeV)		
	3.594	3.60	3.64
$K^{\pm}K_s\pi^{\mp}$	50	20	8
$K^+K^-K^+K^-$	65	23	10
$\pi^+\pi^-K^+K^-$	80	29	12
$\pi^+\pi^-\pi^+\pi^-$	60	21	9

Using branching fractions taken from the above discussion and MC-estimated values of the experimental acceptance, we make the following estimates of the number of expected events in a 20M event BES data sample for different $\eta_c(2S)$ masses, that are given in Table 8. It is clear from Table 8 that a 20M $\psi(2S)$ event sample will enable a definitive search for the $\eta_c(2S)$ over an interesting mass range.

These channels are well studied by the BES detector. For example, we show in Figure 5 the The $KK\pi$ invariant mass distribution for for $\psi(2S) \to \gamma K^{\pm}K_s\pi^{\mp}$ events using the exsisting BES $\psi(2S)$ data sample. The curve indicates the results of a fit that includes the three ^3P χ states, the $\eta_c(1S)$ and a third-order polynomial to represent the background. Note the paucity of events—either signal or background—in the mass region above $M_{\chi_{c2}}$.

2.4.1.2 Studies of the $\chi_{c0\ 1\ 2}$ charmonium states.

The $\psi(2S) \to \gamma\chi_{c0,1,2}$ decays are electric dipole transitions and have branching fractions of order 10%. Thus, a 20M event sample of $\psi(2S)$ will contain ~million event samples of each χ_c state. Hadronic decays of the χ_c states are of interest because they are relatively narrow but massive hadronic states with J^{PC} quantum numbers that differ from those of the 1^{--} J/ψ and $\psi(2S)$ states. Moreover, since B mesons decays to bound $c\bar{c}$ states are important for CP studies, a better understanding of hadronic χ_c decays will be useful for research at e^+e^- B-factories.

The ability of the BES detector for studying these states is illustrated in Table 9, where a number of BES results for χ_c branching fractions are listed together with the current value in the PDG listing [10]. These results are based on the existing BES 3.6M $\psi(2S)$ event sample. Note that with the exception of $\mathcal{B}\chi_{c1,2} \rightarrow p\overline{p}$, where the special power of $p\overline{p}$ formation experiments has great sensitivity, the BES results represent significant improvements on existing measurements. Moreover, the BES measurements indicate that many of the PDG values for important χ_c decay modes are incorrect, sometimes by as much as a factor of four. Our studies indicate that the four charged particle decays are primarily mediated by two-body meson resonance processes. Million event samples of each χ_c state will be valuable for studies of light meson resonance spectroscopy.

2.4.1.3 Studies of the $\psi(2S) \rightarrow J/\psi$ transitions.

$\psi(2S) \rightarrow \pi^+\pi\ \ J/\psi$ transitions.
The dipion invariant mass distribution in $\psi(2S) \rightarrow \pi^+\pi^- J/\psi$ transitions is very different from that expected from phase space, and a number of authors have proposed various theoretical models [31]. The process is pictured as the radiation of two gluons by the quarkonium system as it transfers to the lower energy level, followed by the hadronization of the gluons into pions. There is increased interest in this process because of the problems with the $\Upsilon(3S) \rightarrow \pi^+\pi^-\Upsilon(1S)$, which has a peak at low mass, as well as a peak at high mass. This distribution looks very different than that for $\psi(2S) \rightarrow \pi^+\pi^- J/\psi$, which has a high mass peak, and most theoretical models. The process $\Upsilon(2S) \rightarrow \pi^+\pi^-\Upsilon(1S)$ is similar to $\psi(2S) \rightarrow \pi^+\pi^- J/\psi$, but not exactly the same.

The top panel in Figure 6 shows the $\pi^+\pi^-$ invariant mass distribution from $\psi(2S) \rightarrow \pi^+\pi^- J/\psi$ events in the 3.6M $\psi(2S)$ event sample. The lower panel shows the helicity angle distribution for the decaying $\pi^+\pi^-$ system. The curves are the results of fits using the model proposed in ref. [31]. A significant amount of D-wave is apparent in the data. A larger $\psi(2S)$ data sample would enable a study of the invariant mass dependence of the D-wave component.

The $\psi(2S) \rightarrow \pi^0 J/\psi$ transition.

Table 9: BES results on decays of Charmonium to all charged particle final states

	BES ($\times 10^{-3}$)	PDG ($\times 10^{-3}$)
$\boldsymbol{\chi} \longrightarrow$ two charged particles		
$B(\chi_{c0} \to \pi^+\pi^-)$	42.7 ± 6.4	75 ± 21
$B(\chi_{c2} \to \pi^+\pi^-)$	15.2 ± 1.8	19 ± 10
$B(\chi_{c0} \to K^+K^-)$	34.4 ± 5.1	71 ± 24
$B(\chi_{c2} \to \pi^+\pi^-)$	5.2 ± 2.1	15 ± 11
$B(\chi_{c0} \to p\overline{p})$	1.45 ± 0.50	< 9.0
$B(\chi_{c1} \to p\overline{p})$	0.83 ± 040	0.86 ± 0.12
$B(\chi_{c2} \to p\overline{p})$	0.96 ± 0.54	1.00 ± 0.10
$\boldsymbol{\chi} \longrightarrow$ four charged particles		
$B(\chi_{c0} \to \pi^+\pi^-\pi^+\pi^-)$	17.2 ± 3.5	37 ± 7
$B(\chi_{c1} \to \pi^+\pi^-\pi^+\pi^-)$	4.5 ± 1.0	16 ± 5
$B(\chi_{c2} \to \pi^+\pi^-\pi^+\pi^-)$	8.7 ± 1.8	22 ± 5
$B(\chi_{c0} \to K_s^0K_s^0)$	2.2 ± 0.6	-
$B(\chi_{c2} \to K_s^0K_s^0)$	0.4 ± 0.3	-
$B(\chi_{c0} \to \pi^+\pi^-K^+K^-)$	9.9 ± 2.1	30 ± 7
$B(\chi_{c1} \to \pi^+\pi^-K^+K^-)$	3.0 ± 0.7	9 ± 4
$B(\chi_{c2} \to \pi^+\pi^-K^+K^-)$	4.6 ± 1.0	19 ± 5
$B(\chi_{c0} \to \pi^+\pi^-p\bar{p})$	1.9 ± 0.3	5.0 ± 2.0
$B(\chi_{c1} \to \pi^+\pi^-p\bar{p})$	0.5 ± 0.2	1.4 ± 0.9
$B(\chi_{c2} \to \pi^+\pi^-p\bar{p})$	1.6 ± 0.4	–
$B(\chi_{c0} \to \Lambda\bar{\Lambda})$	0.22 ± 0.15	–
$B(\chi_{c1} \to \Lambda\bar{\Lambda})$	0.12 ± 0.10	–
$B(\chi_{c2} \to \Lambda\bar{\Lambda})$	0.27 ± 0.13	–
$B(\chi_{c0} \to K^+K^-K^+K^-)$	2.2 ± 0.6	–
$B(\chi_{c1} \to K^+K^-K^+K^-)$	0.6 ± 0.2	–
$B(\chi_{c2} \to K^+K^-K^+K^-)$	1.4 ± 0.3	–
$B(\chi_{c0} \to \phi\phi)$	0.83 ± 0.40	–
$B(\chi_{c2} \to \phi\phi)$	1.82 ± 0.55	–
$B(\chi_{c0} \to K_s^0K^+\pi^- + c.c.)$	< 0.6	–
$B(\chi_{c1} \to K_s^0K^+\pi^- + c.c.)$	1.9 ± 0.6	–
$B(\chi_{c2} \to K_s^0K^+\pi^- + c.c.)$	0.41 ± 0.25	–

The ratio of the partial width for the i-spin violating $\psi(2S) \to \pi^0 J/\psi$ transition to that for the $SU(3)$-violating $\psi(2S) \to \eta J/\psi$ transition is of interest because it is directly related to the quark masses via the relation [32]

$$\frac{\Gamma(\psi(2S) \to \pi^0 J/\psi)}{\Gamma(\psi(2S) \to \eta J/\psi)} = 3\left(\frac{m_d - m_u}{m_d + m_u}\right)^2 \left(\frac{m_\pi}{m_\eta}\right)^4 \left(\frac{p_\pi}{p_\eta}\right)^3 \left[1 + \mathcal{O}\left(\frac{m_q}{m_{st}}\right)\right], \quad (24)$$

where m_{st} is a mass characteristic of the strong interactions.

Currently, the precision on this ratio is dominated by the $\psi(2S) \to \pi^0 J/\psi$ measurement, which is based on two measurements with a combined total of 30 events [33]. Preliminary studies with the 3.6M $\psi(2S)$ event sample indicated a similar, statistics limited, sensitivity. A 20M $\psi(2S)$ event sample will provide a commensurate boost in the precision of the measurement of this ratio.

2.4.2 Hadronic decays of the $\psi(2S)$

A-priori, one would think that the hadronic decays of the $\psi(2S)$ should not be particularly interesting. In the standard picture, this state is the first radial excitation of the $^3S_1$ $c\bar{c}$ bound state and its decays are expected to be dominantly $c\bar{c}$ annihilation into three gluons, the same process that is expected to dominate in $J/\psi \to$ hadrons. Since the hadronic final states from both the J/ψ and $\psi(2S)$ decays originate from three gluon states with the same quantum numbers and with nearly the same energy, it seems reasonable to expect that the character of the specific hadronic final states that are produced in $\psi(2S)$ decays should be readily understood in terms of the corresponding J/ψ decay. Comparisons of the hadronic decays of the J/ψ and $\psi(2S)$ test our intuition concerning hadronization processes.

In fact, hadronic decays of the J/ψ and $\psi(2S)$ are very different. Two-body decays to vector plus pseudoscalar mesons, dominant hadronic channels for the J/ψ, are not seen in $\psi(2S)$ decays at very high levels of sensitivity. Likewise vector plus tensor meson decays, which are common for the J/ψ, are absent or strongly suppressed for the $\psi(2S)$. Although decay rates for axialvector plus pseudoscalar meson final states appear to follow expectations, there is a large flavor-$SU(3)$ violation in the strange sector that has completely opposite character for the J/ψ and $\psi(2S)$.

2.4.2.1 The 15% Rule for $\psi(2S)$ Decays

At the parton level, the major difference between hadronic J/ψ and $\psi(2S)$ decays is the value of the $c\bar{c}$ wavefunction at the origin, which is well determined from the dilepton decay rates. This leads to the expectation that the ratio of the J/ψ and $\psi(2S)$ decay branching ratios to any particular final state X_h should, at least roughly, obey the relation

$$Q_h \equiv \frac{\mathcal{B}[\psi(2S) \to X_h]}{\mathcal{B}[J/\psi \to X_h]} = Q_{ee} \equiv \frac{\mathcal{B}[\psi(2S) \to e^+e^-]}{\mathcal{B}[J/\psi \to e^+e^-]} = 0.147 \pm 0.023, \quad (25)$$

where the leptonic decay branching fractions are taken from the PDG listings [10]. This relation, which is sometimes referred to as *the 15% rule*, works within a factor of two or so for many inclusive final states [34] and baryon-antibaryon final states [35], but fails badly for the vector pseudoscalar (VP) final states $\rho\pi$ and $K^*\overline{K}$ [34, 36].

2.4.2.2 The $\rho\pi$ Puzzle

The $J/\psi \to \rho\pi$ decay is the most common exclusive hadronic mode of the J/ψ, with a branching fraction of $1.28 \pm 0.10\%$. Figure 7 shows the $\pi\pi$ mass distribution from tagged $J/\psi \to \pi^+\pi^-\pi^0$ decays. A strong ρ signal, with about 1700 events is apparent; the corresponding branching fraction of $1.3 \pm 0.1\%$, is the largest for any exclusive hadronic J/ψ decay mode. The $J/\psi \to K^*\overline{K}$ decay, which has a branching fraction of $0.92 \pm 0.06\%$ is also an important mode.

In a rather striking contrast, the decays $\psi(2S) \to \rho\pi$ and $K^*\overline{K}$ are strongly suppressed. Figure 8 shows the $\pi\pi$ mass distribution from $\psi(2S) \to \pi^+\pi^-\pi^0$ decays from the same data sample. Here there is barely a hint of a ρ signal. A fit to a ρ plus a smooth background yields 13 ± 6 ρ events. Since the data can be well fit with a smooth background function without any ρ at all, we derive a 90% CL upper limit of $\mathcal{B}[\psi(2S) \to \rho\pi] < 2.8 \times 10^{-5}$. This limit is a factor of 65 below the 15%-rule expectation for this decay. A similar discrepancy is seen for $K^*\overline{K}$ final states, where $\psi(2S)$ decays to this channel are suppressed by at least a factor of 22 below 15%-rule expectations [34].

The current experimental situation for all $\psi(2S) \to VP$ channels is summarized in Table 10, which compares BES results on these decays with PDG values for the corresponding J/ψ branching fractions to the same final states. The righthand column of Table 10 indicates the extent to which the decay is suppressed relative to 15%-rule expectations by a "suppression factor" $\mathcal{S}$, defined as

$$\mathcal{S} \equiv \frac{0.147 \times \mathcal{B}(J/\psi \rightarrow VP)}{\mathcal{B}(\psi_{2S} \rightarrow VP)}, \tag{26}$$

where values of $\mathcal{S}$ greater than unity indicate a suppression. Note that all the $\psi(2S) \rightarrow VP$ modes where measurements exist exhibit some significant suppression, with the notable exception of the i-spin violating decay $\psi(2S) \rightarrow \omega\pi^0$, which has a branching fraction that exceeds that of the strong-interaction-allowed $\psi(2S) \rightarrow \rho\pi$ decay. A strong i-spin violation is also seen for $\psi(2S) \rightarrow K^*\overline{K}$ decays. *Something is suppressing strong $\psi(2S) \rightarrow VP$ decays to a level below that of the electromagnetic interaction.* An order of magnitude increase in the $\psi(2S)$ data sample will enable us to investigate all of the hadronic modes—with the exception of $\psi(2S) \rightarrow \phi\pi^0$—at the level expected for electromagnetic processes.

2.4.2.3 Possible explanations for the $\rho\pi$ puzzle.

A number of mechanisms have been proposed to explain the discrepancy between the J/ψ and $\psi(2S)$ decay rates. One category invokes a scheme that suppress all $\psi(2S)$ two-body meson decays. The other involves mixing of the J/ψ with a nearby vector glueball state, called the $\mathcal{O}$.

Mechanisms that suppress all $\psi(2S) \rightarrow$ two-body meson decays.
Chaichian and Tornqvist proposed a model that has an exponential form-factor suppression of all $\psi(2S)$ decays to two-body meson final states [37]. Pinsky has pointed out that the $\psi(2S) \rightarrow VP$ transitions are hindered relative to their J/ψ counterparts [38]. The suppression factors provided by these mechanisms are not sufficient to account for the larger suppression factors reported by BES, although it may be possible to tune the models to accomodate the new data. However, in these models similar suppressions should apply to all two-body meson final states. Since, as discussed below, no suppression is seen in axialvector-pseudoscalar meson final states, these explanations for the puzzle would appear to be ruled out.

Table 10: A tabulation of measurements $J/\psi \to$ and $\psi(2S) \to$ lowest lying vector- plus pseudoscalar-mesons. The $\psi(2S)$ measurements are from BES.

VP mode	$\mathcal{B}(\psi(2S) \to VP)$ (10^{-4})	$\mathcal{B}(J\psi \to VP)$ (10^{-3})	$\mathcal{S}$ $(= \frac{0.14\mathcal{B}_{J/\psi}}{\mathcal{B}_{\psi'}})$
$\rho\pi$	< 0.28	12.8 ± 1.0	> 64
$K^{*+}K^-$	< 0.3	5.0 ± 0.4	> 23
$K^{*0}\bar{K}^0$	$0.81 \pm 0.24 \pm 0.16$	4.2 ± 0.4	7.3 ± 2.7
$\omega\pi^0$	$0.37 \pm 0.17 \pm 0.06$	0.42 ± 0.06	1.7 ± 0.8
$\omega\eta$	< 0.33	1.58 ± 0.16	> 7.0
$\omega\eta'$	$0.76 \pm 0.44 \pm 0.18$	0.167 ± 0.025	0.32 ± 0.2
$\phi\pi^0$	< 0.15	< 0.0068	
$\phi\eta$	$0.35 \pm 0.19 \pm 0.07$	0.65 ± 0.07	4.3 ± 2.5
$\phi\eta'$	< 0.75	0.33 ± 0.04	> 0.6
$\rho\eta$	< 0.32	0.193 ± 0.023	> 0.9
$\rho\eta'$	< 0.62	0.105 ± 0.023	> 0.2
$\gamma\pi^0$		0.039 ± 0.013	–
$\gamma\eta$	$0.5 \pm 0.3 \pm 0.1$	0.86 ± 0.08	2.5 ± 1.5
$\gamma\eta'$	$1.4 \pm 0.3 \pm 0.3$	4.31 ± 0.30	4.3 ± 1.3

The J/ψ-$\mathcal{O}$ mixing model
Brodsky, LePage and Tuan (BLT) have stressed the fact that $J/\psi \to VP$ decays violate hadron helicity conservation (HHC) and the puzzle is not that $\psi(2S) \to VP$ decays are suppressed but, rather, that the J/ψ decays are anomalously enhanced [39]. An enhancement mechanism involving quantum mechanical mixing of the J/ψ with a nearby vector glueball (a three-gluon state called the Omicron, $\mathcal{O}$) had previously been suggested by Hou and Soni [40]. In the BLT scheme, the $\mathcal{O}$ mass is close to the mass of the J/ψ (within $\sim$ 80 MeV) and far from the $\psi(2S)$. Thus, in addition to $c\bar{c}$, the physical J/ψ contains a three-gluon component. It is this component that is responsible for enhancing the $J/\psi \to VP$ decays.

2.4.2.4 Searches for the $\mathcal{O}$

The BLT scheme makes a definite prediction that the $\mathcal{O}$ should exist with a mass close to that of the J/ψ. The BES group has tried to see the $\mathcal{O}$ two different ways: one by measuring the cross section for $e^+e^- \to \rho\pi$ in the vicinity of the J/ψ resonance [41]; the other, originally suggested by Hou and Soni [40], by examining the $\rho\pi$ mass spectrum in decays $\psi(2S) \to \pi^+\pi^-\rho\pi$.

The $\rho\pi$ energy scan: The cross section scan indicates no sign of an $\mathcal{O}$. The J/ψ line shape determined from the total cross section for $e^+e^- \to$ hadrons provides a good fit to the $e^+e^- \to \rho\pi$ cross section in the J/ψ region. There is no evidence for a second peak in the vicinity that could be attributed to the $\mathcal{O}$. However, it has been shown that these measurements do not place very stringent limits on possible $\mathcal{O}$ masses and widths [42].

The $\rho\pi$ mass spectrum from $\psi(2S) \to \pi^+\pi^-\rho\pi$ decays: Figure 9 shows the $\rho\pi$ mass distribution from $\psi(2S) \to \pi^+\pi^-\rho\pi$ decays. Here the $\rho\pi$ masses, determined from the missing mass recoiling against the $\pi^+\pi^-$, show a pronounced peak that is consistent with the properties of the J/ψ. Superimposed on the plot is the scaled $\pi^+\pi^-$ recoil mass spectrum from a high statistics sample of $\psi(2S) \to \pi^+\pi^-\mu^+\mu^-$ decays plus a constant flat background. The J/ψ lineshape determined from the $\mu^+\mu^-$ events provides a good description for the $\rho\pi$ distribution ($\chi^2/dof = 207/198$). There is no sign of an $\mathcal{O}$ in the mass distribution. However, a careful application of the J/ψ-$\mathcal{O}$ mixing model to these results only results in the limit that $\Gamma_{\mathcal{O}}^{tot} > 4$ MeV. Since the decays of the $\mathcal{O}$ are non-OZI suppressed, its total width should be typical of hadron resonances and this limit is not very restrictive.

The J/ψ-$\mathcal{O}$ mixing model remains as a possible explanation for the $\rho\pi$ puzzle. An order of magnitude increase in the $\psi(2S)$ data sample would provide a sensitivity for $\mathcal{O}$ widths as high as $\Gamma_{\mathcal{O}}^{tot} \sim 15$ MeV, thus covering more interesting possibilities.

2.4.2.5 Other two-body mesonic decays of the $\psi(2S)$

The decays of the J/ψ to the lowest-lying vector plus tensor mesons are also quite strong: the branching fractions to ρa_2, $K^*\overline{K_2^*}$, and ωf_2 are near the 1% level. The BES group has recently reported that the $\psi(2S)$ decays to these final states are also suppressed relative to 15%-rule expectations. Here the level of suppression is about a factor of five; suppressions as drastic as those seen for VP have not yet been established. On the other hand $\psi(2S)$ decays to axialvector psuedoscalar mesons are not suppressed, ruling out models for the $\rho\pi$ puzzle that suppress all two-body meson final states. The BES results for these modes are summarized in Table 11. It should be noted that in contrast to the case for the VP modes, the VT and AP decays do not violate HHC.

2.4.3 Summary

After the BEPC luminosity upgrade is completed, a dedicated few month run at the $\psi(2S)$ can be expected to provide a sample of over 20M $\psi(2S)$ decays. These decays will enable BES to make a definitive search for the $\eta_c(2S)$ over the mass range of interest and will provide million event samples of each of the three triplet χ_c states. These event samples will provide unique opportunities to measure decay properties of the χ states and for light meson spectroscopy.

Moreover, contrary to naive expectations, $\psi(2S)$ hadronic decays *are* of considerable interest in themselves. They are not at all well understood as simple extrapolations from the corresponding decays of the J/ψ. A much larger $\psi(2S)$ data sample will enable a detailed investigation of these processes down to the level of the electromagnetic interactions. The systematic studies of these decays at this level may provide the clues that unravel the

Table 11: A tabulation of measurements $J/\psi \rightarrow$ and $\psi(2S) \rightarrow$ low-lying vector- plus tensor- and axialvector- plus psuedoscalar meson final states. The $\psi(2S)$ measurements are from BES.

VT mode	$\mathcal{B}(\psi(2S) \rightarrow VT)$ (10^{-4})	$\mathcal{B}(J\psi \rightarrow VT)$ (10^{-3})	$\mathcal{S}$ $(= \frac{0.14\mathcal{B}_{J/\psi}}{\mathcal{B}_{\psi'}})$
ρa_2	< 2.7	10.9 ± 2.2	> 5.9
ωf_2	< 1.8	4.3 ± 0.6	> 3.5
$K^{*0}\bar{K}_2^{*0}$ + cc	< 1.8	6.7 ± 2.6	> 5.5
$\phi f_2'$	< 0.47	0.8 ± 0.4	> 2.5
AP mode	$\mathcal{B}(\psi(2S) \rightarrow AP)$ (10^{-4})	$\mathcal{B}(J\psi \rightarrow AP$ (10^{-3})	$\mathcal{S}$ $(= \frac{0.14\mathcal{B}_{J/\psi}}{\mathcal{B}_{\psi'}})$
$b_1^+\pi^-$ + cc	7.4 ± 1.3	3.0 ± 0.5	0.6 ± 0.2
$K_1(1270)^+K^-$ + cc	7.6 ± 1.7	< 1.8	< 0.35
$K_1(1400)^+K^-$ + cc	< 2.7	5.0 ± 1.3	> 2.7

$\rho\pi$ puzzle. The understanding of the source of this puzzle will likely lead to important insights into hadronic physics.

3 Current Status of BEPC and BES-II

3.1 BEPC

The BEPC collider has been upgraded with improved rf and emittance control, and the implementation of a single interaction point. The upgraded BEPC collider is performing well, reaching a peak luminosity during commissioning runs of 6×10^{30} cm^{-2}sec^{-1} at a center of mass energy of 4.03 GeV. This is more than an order of magnitude greater than the peak luminosity achieved by MARK-III at SPEAR. Accelerator-induced backgrounds have been substantially reduced. A special attempt will be made to maximize luminosity at lower energies for the proposed R scan.

An initial study of obtainable beam currents and luminosities as a function of beam energy has been done. Table 12 summarizes the results of this study. Down to $E_{cm} = 2$ GeV, beam currents and luminosities remain good, indicating that an R scan down to this energy is realizable. Below $E_{cm} = 2$ GeV, currents and luminosities drop by about an order of magnitude. At these energies, an R scan is still feasible, but with fewer data points.

Table 12: Results of the low-energy test of BEPC.

E (GeV)	ΣI (mA)	$\mathcal{L}$ (10^{30} cm^{-2}sec^{-1})	Lifetime (hr)
1.00	6.05	0.157	> 5
1.10	9.45	0.336	4
1.20	9.6	0.3	4
1.25	12	0.47	6.5
1.30	13.1	0.685	8
2.015	47.7	5.705	5
2.50	33.6	4.5	5

During the 1996-97 run, BES received 25% of the available beam time. This does not include start-up and injection time or the R scan study.

The performance of the linac is expected to improve with the replacment of six klystrons. This will allow for more stable injection, with improved luminosities at lower energies.

3.2 BES-II

In 1995-96, BES underwent an upgrade that included a new Vertex Chamber (VC), new Main Drift Chamber (MDC-II), new Time of Flight system (TOF), and improved high voltage distribution and gas flow in the Barrel Shower Counter (BSC) and Endcap Shower Counter (ESC). The MDC-II was completed in late 1995 and installed in BES-II as part of the general upgrade. BES-II began taking data in early 1996. The commissioning run was successful, with the upgraded components functioning as expected, and at a level exceeding BES-I. The performance of individual detector subsystems is summarized in Table 13. The MDC-II performed well at first, but because of the defective feedthroughs, this chamber's performance has degraded.

Table 13: Comparison of the performance of BES-I and BES-II.

Element	Quantity	BES-I	BES-II
VC	σ_{xy}	400 μm (CDC)	90 μm
MDC	Efficiency	96% (L8)	85-95% (L1-9)
	σ_{xy}	200-250 μm	190-210 μm
	σ_z	6 mm	5.88 mm
	dp/p	$1.76\%\sqrt{1+p^2}$	$1.78\%\sqrt{1+p^2}$
TOF	σ_t	375 ps	172 ps
	Atten. length	1-1.2 m	3.5-5.5 m
BSC	$\sigma_E/\sqrt{E}$	25.2%	20.6%
	σ_z	4.5 cm	2.4 cm
ESC	$\sigma_E/\sqrt{E}$	24.4%	21.7%
MU	Efficiency	95%	95%
	σ_z	5.5 cm	5.5 cm

The VC replaced the Central Drift Chamber (CDC) in BES-I. The VC was constructed at CSU, and the VC front-end electronics were built at UH. The chamber achieved a single hit resolution of 70 μm in a bench test using cosmic rays. Once installed in BES-II, a resolution of 90 μm was measured (Figure 10). The poorer resolution is due mainly to inherent timing uncertainties in the trigger. Even at this level, however, the VC performance is considerably better than the CDC.

The performance of the MDC-II, although compromised by the feedthroughs, has been comparable to MDC-I. Figure 11 shows momentum distributions from Bhabha events in BES-I and BES-II. The momentum resolution is $\approx$ 50 MeV at 1.5 GeV in BES-II. Single-hit spatial resolutions and efficiencies are comparable to BES-I.

The new TOF system is performing much better than its predecessor. Figure 12 shows the TOF resolution. The mean resolution is about 172 ps.

During the upgrade, the several broken channels in the shower counter were recovered and the HV distribution was upgraded. Figure 13 shows the energy resolution in the Barrel Shower Counter and Figure 14 shows the energy resolution in the Endcap Shower Counter. The resolution of the BSC

$\sigma_E/\sqrt{E}$ is 20.6% in BES-II compared to 25.2% in BES-I. In the ESC, the energy resolution improved to 21.6% in BES-II from 22.6% in BES-I.

The unmodified muon counters continue to perform well after the upgrade.

4 MDC-III

As discussed above, we have revived MDC-II by reconfiguring the HV distribution so that no feedthrough has to stand off more than ~ 2 kV. We expect the reconfigured chamber will have a lifetime sufficient to permit measurements of R in 1998 and 1999. Nevertheless, the repair of MDC-II is at best a temporary solution. Tests performed on spare feedthroughs indicate that even at the lower voltage, the feedthroughs continue to degrade. In order to ensure the continuation of the BES physics program, it is necessary to construct a new drift chamber. The new chamber is expected to have a useful working life of at least five years.

Other options have been explored. Removing the existing chamber and replacing the wires and feedthroughs would be a time-consuming job, during which BES data taking would be suspended. Because BES is the major experiment at IHEP, down-time for BES work will be minimized by not rolling BES out of the beamline, which would shut down all operation of BEPC and the synchrotron radiation experiments at BSRF. Construction of a new chamber can proceed while BES continues to take data with the temporarily repaired MDC-II. Rebuilding the first drift chamber, MDC-I, has also been explored. It has been determined that because of construction techniques used, removal of the outer cylinder would damage it beyond use. It has therefore been determined that the only option is the construction of a new chamber. We propose to build a copy of MDC-II, saving engineering time and costs.

4.1 Performance Requirements of the Drift Chamber

A feature common to nearly all high energy colliding beam experiments is a large volume charged-particle tracking chamber. Immersed in a coaxial magnetic field, these chambers yield trajectory and momentum information for charged particles traversing their fiducial volumes. They also provide energy loss information for particle identification and are used as inputs to trigger systems.

The principle requirements of the BES Main Drift Chamber are the following:

1. Good solid angle acceptance as close to 4π as possible;
2. High efficiency; single wire efficiency close to 100%;
3. Good spatial resolution in both the $r - \phi$ plane and the $z-$ coordinate along the axis of the chamber;
4. Good momentum resolution. Both terms contributing to the momentum resolution – the spatial resolution and the multiple scattering – have to be small;
5. Good dE/dx resolution and large sampling frequency;
6. Good two-track resolution. This is important with the single-hit electronics used at BES;
7. Ease of integration into the trigger;
8. Ease of track reconstruction and pattern identification to save CPU time in off-line analysis; and
9. Long lifetime, ease of maintenance, and ease of construction.

These are the same requirements imposed on MDC-II, which was largely successful, save for the problem with the feedthroughs. To save engineering costs and development time, the new chamber will be a copy of MDC-II.

4.2 Design Considerations

The design for the drift chamber includes a small drift cell size, a symmetrical cell arrangement, compensating field shaping, and improved feedthrough design and high voltage distribution. These are each discussed in detail below.

4.2.1 Drift Cell Design

The new chamber will have 804 cells and 3216 sense wires distributed in 10 layers. This produces a small drift cell that has the following advantages:

• *Good spatial resolution.*

The spatial resolution depends on the tolerances of the machining and assembly, the uncertainties in the electronics readout system, fluctuations in the positions of the primary electrons, and diffusion of the primary electrons when they drift to the sense wires. The main effect on the intrinsic spatial resolution is diffusion. The average displacement due to electron diffusion perpendicular to the field is proportional to $\sqrt{Dx}$, where D is the diffusion constant and x is the drift distance. The average displacement parallel to the field due to diffusion is proportional to $\sqrt{Dx/E}$, where E is the electric field. In both cases, a small cell size limits the effect of diffusion. In the latter, since the voltage possible is often limited by external concerns (breakdown on components outside the chamber gas volume, etc.), the smaller cell size leads to a higher field, and consequently to less diffusion. Finally, D is itself proportional to $1/E$, so that a small cell size again contributes to reducing the effects of diffusion.

• *Improved momentum resolution.*

There are two terms that contribute to the momentum resolution: the first is from the spatial resolution, the second is from multiple scattering. The transverse momentum resolution in the $r - \phi$ plane is given by

$$\left(\frac{\sigma_{p_t}}{p_t}\right)^2 = \left(\frac{\sigma_{p_t}}{p_t}\right)^2_{spatial} + \left(\frac{\sigma_{p_t}}{p_t}\right)^2_{mult.scat.} \tag{27}$$

For the first term we have approximately

$$\left(\frac{\sigma_{p_t}}{p_t}\right) = \frac{3.3 \times 10^3}{BL^2}\sigma(x)\sqrt{\frac{720}{N+5}} \tag{28}$$

where $\sigma(x)$ (in cm) is the spatial resolution, B (in T) is the magnetic field strength, p_t is the transverse momentum, L (in cm) is the path length, and N is the number of sampling points. Obviously, good space resolution implies good momentum resolution.

• *Improved drift velocity saturation.*

The position of the track traversing the chamber is determined by the drift time. It is desirable to have a constant drift velocity through the drift volume so that we can use the simple formula for the drift distance, $s = vt$, in the drift region of the cell. In practice, the drift velocity is not constant but is a function of the field strength. Near the sense wire (radial region) the electric field is proportional to $1/r$. Away from the sense wire the field is nearly constant.

In the design of the drift chamber we use two methods to make the drift velocity as nearly constant as possible:

1. Optimize electrode (field, guard, potential, and sense wire) positions and potentials to achieve uniform electric field lines in the drift region of the cell. We have calculated the electric field in our drift cells, and show the result for two cells in Figure 15. A nearly uniform field is achieved over most of the cell.

2. Select a gas mixture in which the drift velocity is saturated when the electric field is greater than some critical value, E_c. In our chamber we will use the gas mixture (HRS gas):

$$89\% \text{ Ar} + 10\% \text{ CO}_2 + 1\% \text{ CH}_4.$$

   The critical value for this gas is $E_c = 700$ V/cm (based on prototype studies done at IHEP). According to the results of our electric field calculation, the electric field is 830 to 850 V/cm in the radial mid plane of the cell, which is close to E_c.

In the proposed cell design, we can get higher fields, better saturation, and, thus, more stable running. We prefer to operate the chamber in a saturated condition so the performance is less sensitive to pressure and temperature changes, high voltage stability, variations in gas composition, and machining tolerances.

• *Improved two track resolution.*

The two track resolution refers to the ability of the chamber to identify two neighboring tracks that traverse the same cell. In the small cell design, we reduce the muti-hit probability. In practice, because space constraints in the inner few layers prevent a substantial decrease in cell size, it is envisioned that multi-hit electronics could be used. Moreover, the Vertex Chamber (installed during the upgrade) has a very small cell size (4 mm) and excellent spatial resolution that will help resolve overlapping tracks.

- *Reduce the Lorentz angle.*

The electrons which drift to the sense wire perpendicular to the axial field will feel the Lorentz force that arises from the solenoidal magnetic field. In drift cells which have uniform electric field the Lorentz force deflects the drift path by the Lorentz angle α :

$$\tan\alpha = \left(\frac{1}{K}\right)\left(\frac{B}{E}\right)V \tag{29}$$

where K is a constant, B is the magnetic field strength, and V is the electron drift velocity. The magnetic field changes the drift path of the electrons, distorts the linear relationship between the drift distance and time, and degrades the space resolution. It also distorts the dE/dx collection region, thus decreasing dE/dx resolution. Smaller drift cells with stronger electric fields reduce the Lorentz angle.

4.2.2 Symmetry of the MDC Cell Arrangement

From a tracking and triggering point of view, the drift chamber should have n-fold symmetry. This simplifies the trigger circuit design and the off-line track reconstruction program. From the physics point of view, the relative position of the cells from layer to layer should be randomized in order to get good resolution for all tracks that have different momenta, since near the sense wire spatial resolution is worse due to ionization statistics and the non-linear relationship between the drift time and the drift distance. This has a detrimental effect on the resolution of high momentum tracks such as the two track decays e^+e^-, $\mu^+\mu^-$, etc.

A carefully ‘random’ configuration guarantees that there is no region of the chamber where a track will pass through several cells close to the sense wires. This produces an equal spatial resolution for high and low momentum tracks. In our design a compromise is made. The whole chamber has a four-fold symmetry, with the inner four layers having eight-fold symmetry. In every quarter the layer to layer pattern is random.

- *Improved Feedthrough Design*

The functions of the feedthroughs in the drift chamber are to position the wires accurately, to insulate the wires from the endplates, to bring high voltage into the chamber, and to allow the signals out. The MDC-II feedthroughs were successfully molded to the required mechanical tolerances. A small machined plastic insert was inserted into the end of each feedthrough to position the wires accurately. For the new chamber, we will again use this design, but will use a material with better molding and electrical properties than the Delrin used in MDC-II. One candidate material is glass-filled Celanex 3310, which CSU has successfully used to mold feedthroughs for the BaBar drift chamber. Figure 16 shows the design of the MDC-III feedthroughs.

• *High Voltage Distribution Boards*

The initial design of MDC-II called for voltage to be applied to the field wires only. While this produced the required field with the sense wires at ground potential, it also produced a large field gradient through the field wire feedthroughs. It was this large gradient that accelerated the degradation of the Delrin feedthroughs. Based on that experience, we will divide the applied voltage between the field wires and the sense wires. Since the voltage on the potential and guard wires will also have to be modified, there is a total of four separate voltages that will have to be supplied to the chamber. The HV distribution boards will mount directly on one of the endplates, and will contain current limiting and filtering circuitry. The field wire distribution circuit will contain a voltage divider to slightly decrease the voltage applied to wires at smaller radii in a cell to compensate for the changing size of the drift cell.

• *Temperature and Gas Pressure Corrections*

Gas gain will change with fluctuations in the temperature of the environment as

$$\frac{dM}{M} = K_1 \left(\frac{dT}{T}\right) \tag{30}$$

where M is the gas gain, T is the temperature in Kelvin and K_1 is a constant. The gain will change with gas pressure as well. Some references claim that the proportionality is linear

$$\frac{dM}{M} = K_2 \left(\frac{dP}{P}\right) \tag{31}$$

where P in the pressure and K_2 is another constant; however, some references claim that the gain is inversely proportional to pressure. To clarify the situation a prototype has been made to determine the dependence and determine the relevant constants. Temperature and pressure transducers will be mounted on the chamber to monitor T and P.

4.2.3 Basic Design of the New Drift Chamber

• *Configuration of the Drift Cells*

The Main Drift Chamber will have 10 layers (as shown in Figure 17) with the number of cells given in Table 14. There are four sense wires in each cell to measure both timing and dE/dx information.

Table 14: Main Drift Chamber cell positions.

Layer number	1	2	3	4	5	6	7	8	9	10
Number of cells	48	48	64	56	68	80	92	104	116	128
Angular coverage per cell (degrees)	7.5	7.5	5.6	6.4	5.3	4.5	3.75	3.46	3.1	2.8
Half width of cell at cell center (mm)	14.1	19.2	18.4	26.0	26.1	26.1	26.1	26.1	26.1	26.1
Radius of cell center (mm)	215	295	375	465	565	665	765	865	965	1065
Wire orientation	U	A	V	A	U	A	V	A	U	A
Gap between layers (mm)	35	30	30	30	30	30	30	30	30	40

• *Drift Cell*

The positions of the electrodes (wires) in a drift cell are shown in Figure 18. In layer 1 the drift cells are 12 field wires thick; layers 2 and 3 are 11 field wires thick; and layers 4 - 10 are 15 field wires thick. There are four sense wires in each cell in every layer. The sense wires are gold-plated tungsten, 30 μm in diameter. The field wires are Be-Cu, 178 μm in diameter. By adjusting the high voltage on the field wire we can acheive an almost uniform drift field E except in the region near the wire surface. The voltage should be high enough so that E exceeds E_c, the critical value for the saturated drift velocity. At the two edges of each layer a thicker wire is used in order to reduce the electric field strength at the wire surface so the field gradient will be smaller. The potential wires play an important role in the drift chamber: they limit the sensitive region for each sense wire, reduce cross-talk between sense wires, increase the electric stability of the wire, and control the gain via adjustment of their potentials. In order to reduce the distortion of the drift field near the cell edge and adjust the gain of the outer sense wires, one or two guard wires are used at the edge of each layer. The distribution of the potential fields is shown in Figure 15.

- *Left-Right Ambiguity*

The position of charged particles traveling through the drift chamber is determined by measuring the drift time. We cannot distinguish whether the particles passed to the left or the right side of the sense wire by using the time signal alone. In order to solve this ambiguity we can use double sense wires or staggered sense wires. In the new drift chamber staggered wires will be used. The sense wires are alternately displaced $\pm$ 350 μm from the center of the cell. The principle for selection of the size of the displacement is that it should be small enough to retain electrostatic stability which is inversely proportional to the displacement.

- *z-Coordinate Measurement*

The stereo wire method will be adopted in the new drift chamber. The basic idea of the this method is the following: the direction of the wires in each layer is deflected by a small angle (2.2^o to 5^o in our case) to the left (U layer) or right (V layer) from the axial direction consecutively layer by layer. The z-coordinate can be calculated from the time of the signal's arrival and the geometry. The advantage of this method is that it doesn't require high level electronics and the gain can be made consistent with dE/dx measurements. The disadvantage is that the CPU time which has to be used to calculate the z coordinate is too long for that information to be used in the trigger.

- *Tension and Wire Types*

The materials, tensions and sags for the different wire types are shown in Table 15.

- *Cell Distribution*

The cell distribution for each layer is shown in Table 14. There are 11

Table 15: Main Drift Chamber wire materials.

Wire type	Material	Dia. (μm)	Tension (g)	Sag (μm)
Sense	Au-plated W	30	100	77
Potential	Inconel-600	100	500	78
Field	Be-Cu	178	500	229
Thicker Field	Be-Cu	220	600	292
Guard	Inconel-600	100	500	78

wires per row for layers 1 to 3 and 15 wires per row for layers 4 to 10. The total number of cells is 804 and the total number of sense wires is 3216. This chamber has four-fold symmetry. For the first four layers the symmetry is eight-fold. The cell positions from layer to layer are 'random' in every quarter of the chamber.

4.2.4 Mechanical Tolerances

The space resolution of the drift chamber depends on the tolerances of manufacture and assembly, fluctuations in the environment, the walking (with time) of the readout electronics, and the intrinsic resolution. We have to keep the mechanical tolerances as small as possible in order to achieve good spatial resolution.

• *Endplates*

The crucial components in the MDC-III are the endplates, which locate and support the guard, field, and sense wires for the ten layers of drift cells. The endplates are 2.2 m (89 in) in diameter. Table 16 gives the preliminary specification of the MDC-III layout. There are approximately 23,000 holes in each endplate; each endplate will also have approximately 3,000 blind tapped holes for mounting electronics. To achieve the position resolution required of the MDC-III, holes for the feedthroughs for the field and sense wires must be placed with a precision of ± 0.018 mm (± 0.0007 in). Meeting this tolerance for the very large number of holes over the very large area of the endplates will be a challenging undertaking.

The two endplates of the new drift chamber will be made of hard Al 6061 of 4 cm thickness. They are mounted on the outer cylinder via the outer

Table 16: MDC-III Preliminary Specifications.

Layer number	1	2	3	4	5	6	7	8	9	10	Totals
No. of Cells	48	48	64	56	68	80	92	104	116	128	804
Half Width (mm)	14.1	19.2	18.4	26.0	26.1	26.1	26.1	26.1	26.1	26.1	
Opening Angle (deg)	7.50	7.50	5.63	6.43	5.29	4.50	3.91	3.46	3.10	2.81	
No. Sense Wires	192	192	256	224	272	320	368	416	464	512	3216
No. Field Wires	576	528	704	840	1020	1200	1380	1560	1740	1920	11,468
No. Potential Wires	240	240	320	392	476	560	644	728	812	896	5308
No. Guard Wires	144	96	128	224	272	320	368	416	464	512	2944
Total Number of Wires											22,936

rings which are welded to the outer cylinder. The outer cylinder is also Al 6061, 2 cm in thickness and about 2.3 m long. All the wires are positioned via feedthroughs in the endplates. The relative position of the two endplates can be adjusted and surveyed using the optical holes. The standard reference is the inner surface. The tolerances of the endplates are given in Table 17.

Alignment of the endplates will depend on the accuracy of the optical holes. These need to be well positioned in order to align the endplates to the required tolerance. The ultimate resolution of the chamber will depend on the accuracy of the feedthrough placement, both the positions of and the sizes of the holes that the feedthroughs are placed into. The tolerances of the optical holes and the feedthrough holes are given in Table 18.

Table 17: MDC-III endplate precision requirements.

Flatness of the reference surface	250 μm
Parallelism of the two surfaces	250 μm
Tolerance of the thickness	250 μm
Assembling parallelism of the two endplates	250 μm
Alignment of the x and y axes of the endplates	250 μm

Table 18: MDC-III feedthrough and optical hole tolerances.

Diameter of feedthrough holes	± 18 μm
Position of feedthrough holes relative to center of endplate	± 50 μm
Diameter of optical holes	± 16 μm
Position of optical holes relative to center of endplates	± 30 μm
Maximum horizontal displacement between the center of the top optical hole and the center of the bottom optical hole	± 50 μm

4.2.5 Fabrication Plans for the Endplates and the Outer Cylinder

We propose to use the Engineering Shop Facility (ESF) of the University of Hawaii's School of Ocean and Earth Science and Technology (SOEST) to build the endplates and the outer cylinder. The ESF has experience with building large projects in support of SOEST's deep sea and environmental research program. They have experience with high pressure devices with multiple penetrations for windows and connectors; in high pressure deep sea systems, precision and close attention to detail is crucial for success.

Figure 19 is a photograph of a complex high pressure vessel that ESF recently designed and built for a joint venture with the Hawaii Natural Energy Lab and Pacific International Center for High Technology Research. The vessel inside dimensions are 60 cm in diameter by 300 cm long, and it operates at 3000 psi. There are 16, 10 cm diameter optical windows. Internally, there is a high pressure manometer bar which moves on a ball bearing trackway and is positioned with a digital stepping motor. There is a large injector in the base of the vessel for the injection of liquid carbon dioxide. All design, fabrication, and assembly, including the vessel, view ports, internal instrumentation, and injectors were handled in ESF shop. The device was built on schedule, within budget, and performs according to specification.

For the endplate disks, two pieces of 6061-T651 aluminum stock with inner and outer radii machined and surfaces Blanchard ground to specifications will be purchased from a supplier on the mainland. At least one supplier capable of providing these items has been identified and has expressed an interest in providing these parts for a cost that is consistent with our budget.

The specified tolerance requires that the maximum deviation from the specified center of any of the wire holes will be no more than 18 μm from the reference point, the center of the disk. This requires the thermal control of the workspace to better than $\pm 1.5^{\circ}$C. Perpendicularity of the holes and the hole diameter must also be closely controlled. ESF engineers have established that they can meet the dimensional requirements of this project.

The drilling will be accomplished with the disk being rigidly held on a custom-made support table with the center axis of the disk vertical. A special CNC drilling fixture would be used to position a production high speed drill head in both the x- and y-axis being positioned by digital stepping motors, and moved by ball screws on a precision traverse. Linear encoders will be used to maintain the required level of precision. These traverses would position a production drill head, a small compact high speed unit with a canned drilling cycle and load sensing ability. Custom-made drills will be used in order to maintain accuracy and a high production rate. The drilling fixture would be able to drill all of the holes in a 1/8th segment of the total disk area. Thus, the drilling fixture would be re-positioned 8 times during the production process by rotating it accurately on a pivot point located in the center of the disk. Repositioning will be accomplished by unclamping the fixture from the disk and rotating it (by 45°) to the next position. The position accuracy of positioning will be maintained by the use of an auto collimator and a master polygon.

The outer aluminum cylinder will be purchased from an outside shop either in Hawaii or on the mainland. We have found a vendor in Hawaii experienced with fabricating large vessels. They have examined the drawings for the outer shell and have determined that they could build it within tolerances and for a cost within the amount that we have budgeted for this part of the project. If approved, we will also solicit quotes from vendors on the mainland.

4.2.6 Gas Mixture

Selection of the gas is very important. The requirements of the drift chamber gas the following:

1. Large gain but low operating voltage;
2. Satisfactory and saturated electron drift velocity; low critical field;
3. Small Lorentz angle;
4. Small diffusion coefficient;
5. Large dE/dx energy loss for charged particles; and
6. Long lifetime.

A noble gas has been chosen as the main component of the drift gas since it has a high first Townsend coefficient, hence greater gain, than organic gases that are rich in non-ionizing (rotational and vibrational) energy levels. The most favored noble gas is Argon since it is inexpensive. Photons are emitted when the excited argon is de-excited and some electrons (called secondary emission) are emitted due to collisions of the photons with argon ions and with the atoms of the cathode. A gas with a molecule containing many atoms must be added to argon as a quenching agent to absorb the photons in a quite wide energy range. We use CO_2 in our gas mixture since it has a long lifetime and is inexpensive. CO_2 has a weak secondary emission effect due to the simplicity of its molecule. A small quantity of CH_4 is also added to increase the quenching ability. The gas mixture that we propose for our chamber is HRS gas:

$$89\%\ \mathrm{Ar} + 10\%\ \mathrm{CO_2} + 1\%\ \mathrm{CH_4}.$$

Table 19 shows the characteristics of this gas mixture.

Table 19: MDC-III gas mixture characteristics.

Composition	89% Ar + 10% CO_2 + 1% CH_4
Gain	$\approx 10^4$ (proportional mode)
Saturated drift velocity	5 cm/ms
Critical drift field strength	$E_c = 700$ V/cm
Lorentz angle	$\approx 17^o$
Diffusion coefficient	≈ 100 mm/$\sqrt{\text{cm}}$
Most probable dE/dx	$\approx$1/37 KeV/cm

4.3 Feedthroughs and Solder Pins

The feedthroughs and solder pins are critical elements of the MDC-III the must be fabricated to high mechanical and electrical standards, yet also allow for efficient and robust construction. CSU proposes to fabricate these elements. The final assembly steps of gluing the solder pins into the feedthroughs and the stringing of the chamber will be done at IHEP.

This section begins with a review of the problems associated with the MDC-II feedthroughs and CSU efforts to identify those problems. We then describe the steps we will take to prevent similar problems in the MDC-III feedthroughs.

4.3.1 MDC-II Feedthroughs

The poor performance of the BES MDC II has been traced to the feedthroughs. While every effort was made to produce high-quality parts by constant inspection and testing, the change of a mold parameter by the injection molding company produced an unseen fault in the feedthroughs. This fault did not manifest itself until after the feedthroughs had been installed and the chamber operated for several months.

4.3.1.1 Choice of Material

Material choice for the MDC-II feedthroughs was driven by cost, ease of production, ability to hold the required mechanical tolerances, and electrical characteristics. Delrin$^{\mathrm{TM}}$ fulfilled all these requirements, as evidenced by its successful application in many previous experiments (Mark III, HRS, and BES-I for example). After consultation with IHEP about candidate materials we chose injection molded Delrin$^{\mathrm{TM}}$ since that would allow the feedthroughs to be produced most economically. The grade of Delrin$^{\mathrm{TM}}$ chosen was 500P, a moderate viscosity thermoplastic with good injection molding characteristics.

4.3.1.2 Production of the MDC-II Feedthroughs

The feedthroughs were produced in Ft. Collins during summer 1994. They were made by a local molding company that had been recommended to CSU by physicists at the University of Colorado. Their recommendation was based on successful parts the company produced for prototype SSC intermediate tracking chambers. Several dozen prototype feedthroughs were produced and sent to IHEP for inspection and testing. Only after we received approval from IHEP did we begin producing feedthroughs for MDC-II.

Dimensional tolerences on the feedthoughs were quite severe, well below DuPont recomendations for injection molded Delrin$^{\mathrm{TM}}$. In order to produce parts consistently within specifications, the molder adjusted the parameters on the injection molding machine in accord with industry practice. For example, the DuPont Delrin$^{\mathrm{TM}}$ molding guide suggests increasing injection pressure, among other things, to avoid shot-to-shot dimensional variations. However, because the feedthroughs were required to have no taper, it was very difficult to extract them from the mold. To solve this problem, the molding guide suggests, among other things, decreasing injection pressure. This illustrates the difficulty in balancing temperatures, pressures, and times in the injection cycle to produce parts within specifications that could be removed from the mold. The final machine settings had cycle time and injection pressure within recommended ranges, cylinder temperature slightly below recommended, and mold temperature well below recommended by DuPont. At the time of production, the molder gave us no indication that the mold temperature was set below these recommendations. The dimensions of the feedthroughs were, however, within our specifications. It should also be noted that decreasing the melt temperature is one of the recommendations for avoiding voids, a common problem in injection molded Delrin^{TM}.

The feedthroughs were taken to CSU where they were cleaned in an unheated ultrasound bath using ethanol and dried in room temperature air. Samples from the beginning and end of each molding run were examined for dimensional stability (about 4% of the feedthroughs were examined). Because of the well-known problem of voids in molded Delrin^{TM}, we visually inspected the feedthroughs very carefully, cutting many of them open to look for voids, which were not found. A machined Delrin^{TM} insert was placed in each feedthrough to position the wire. The inserts were cleaned using the same procedure as the feedthroughs. Excess plastic was removed during inspection, and each insert was required to have a clean hole of the appropriate diameter. Concentricity measurements of the insert inner diameter to the feedthrough outer diameter were made for the 4% of the feedthroughs we inspected. A small sample of the feedthroughs was placed on high voltage for several days and no current draw was seen. The feedthroughs were bagged and shipped to IHEP in September 1994.

4.3.1.3 Performance of MDC-II

A few months after MDC-II was commissioned, the outer layers began drawing high amounts of dark current and the chamber became exceptionally noisy in specific areas of the detector. The high voltage distribution system was suspected as a cause of the former problem, and shower counter crates as a cause of the latter. Both were worked on, and the situation improved initially. However, the performance of MDC-II continued to degrade, and the feedthroughs were now considered suspect. In February 1997 BES collaborators at IHEP placed about 100 unused feedthroughs in the MDC-II prototype with solder pins and applied 4 kV to the pins. The current in the prototype began to rise after 21 days, reaching 80 microamps 16 days after that. Several of the feedthroughs sparked through the Delrin^{TM} wall.

4.3.1.4 HV Tests at CSU

After we learned of the potential problem with the feedthroughs from IHEP, we immediately set up another test in March 1997 at CSU using overproduction feedthroughs that never left CSU. These feedthroughs had been cleaned and handled in the same manner as those sent to IHEP, and had been stored in a sealed plastic bag. The results were qualitatively the same as from the IHEP test, but the maximum current was only about 10 microamp total. One of the feedthroughs sparked through the Delrin™ wall. The current in the CSU test seems to depend strongly on humidity (Figure 20).

4.3.1.5 SEM Work at CSU

Two small groups of MDC-II feedthroughs were sent back to CSU from IHEP. One group was unused, and the other was used in the prototype test. Following a discussion with DuPont where it was learned that injection molding Delrin™ produces a skin on the molded part, we decided to examine the surfaces of the returned feedthroughs. For this examination we used a scanning electron microscope (SEM). Examination of feedthroughs returned from IHEP and feedthroughs that never left CSU show two distinct features: cracks and pits.

Common to all feedthroughs are very small cracks on the inner and outer surfaces. These cracks are in general less than one micron wide, and their distribution is not uniform. There are relatively large areas that show no surface cracking. The used feedthroughs from IHEP have these small cracks, as well as relatively large cracks, 10 microns or more wide (Figures 21 and 22). Used feedthroughs from CSU do not show these large cracks, with one exception: there are large cracks near the puncture in the CSU feedthrough that sparked, indicating that the release of energy into the plastic by an electrical discharge of less than 4 kV is sufficient to damage the plastic.

4.3.1.6 Analysis by DuPont

Several feedthroughs were sent to DuPont, who agreed to examine them. Two used feedthroughs from IHEP, two unused feedthroughs from IHEP, and two unused feedthroughs from CSU were sent. DuPont examined the crystal structure of the Delrin^{TM}, and reached the same conclusion on all six feedthroughs. According to their analysis, either the mold temperature was too cold, or the temperature of the molten Delrin^{TM} was too low when the feedthroughs were made. The first conclusion has been confirmed by the molder. Because the feedthroughs are long thin parts with straight sides, they would not release from the mold when molded at the proper temperature. In order to get the feedthroughs out of the mold, the molder reduced the temperature of the mold below the DuPont recommended range. This resulted in the Delrin failing to crystallize properly at the surface of the feedthroughs. The molder claims no knowledge of ill effects caused by varying temperatures in the molding process. Indeed, adjustment of molding parameters is an industry-wide practice, used to compensate for invariable differences in plastics, injection molding machines, molds, and ambient environmental conditions.

4.3.1.7 Long-term Effects

As a result of the improper crystallization, the Delrin^{TM} would continue to shrink over a long term, possibly months. This continued shrinkage leads to a buildup of stress in the plastic. The small (micron sized) cracks on the surfaces of the feedthroughs are probably a response to this stress. Micro-discharging inside these small cracks in the field wire feedthroughs produces further damage to the Delrin^{TM} through thermal scission of the polymer chains, chemical attack by radicals produced in the discharge, and damage from the inpact of electrons and ions. The third mechanism is thought to be the most important mechanism of damage to plastics by electrical discharge[43].

Possible mechanisms for damage were investigated using energy dispersive spectroscopy (EDS). A longitudinal cross-section of a damaged feedthrough was examined for contaminates inside a deep crack. Aluminum was found inside the crack, but not in undamaged material adjacent to the crack. Since the outer surface of the feedthrough was in contact with the aluminum endplate of MDC-II, this is evidence of damage caused by ions liberated from the endplate during electrical discharge.

Continued micro-discharging in the plastic eventually punctures the feedthrough, rendering the feedthrough incapable of holding high voltage. In MDC-II, 33 field wire feedthroughs were found to have been severely damaged. Of these, 17 have been pulled and the wires and feedthroughs replaced using a 'sacrificial wire' technique. The remain 16 are either in positions difficult for restringing (*e.g.* layer 10) or are at the edge of drift cell, where simply disconnecting the wire from HV is considered an acceptable alternative to the risks associated with restringing.

4.3.2 MDC-III Feedthrough Design

The feedthroughs of the Main Drift Chamber provide support for the wires, position the wires, and insulate the wires from the grounded endplates. These requirements place demanding constraints on the feedthrough specifications. They must be able to tolerate electric fields of several kV/cm without breaking down, and yet be able to position the wires to an accuracy of a few tens of microns. Materials and fabrication techniques must be chosen carefully. The design of the MDC-III feedthroughs is essentially the same as those in MDC-II. We do, however, propose to make the new feedthroughs out of a different material.

The proposed feedthrough design is shown in Figure 16. The feedthrough specifications are shown in Table 20. The body of the feedthrough is a long, relatively thin piece that presents a fabrication challenge. The outer diameter must be maintained within the specified tolerance for the entire length of the shaft. This is necessary for wire placement and for a gas seal. We have found that the most reliable and most inexpensive way to produce this part is by injection molding. Our material of choice is a glass-filled polyester such as Celanex 3310. This material has mechanical properties that allow us to achieve the required tolerance, and the electrical properties to stand off the applied high voltage. The inner diameter along most of the length of the body is not a critical dimension since the solder pin, which is inserted into this hole, does not position the wire. The wire is positioned by a small precision insert that is inserted into the end of the feedthough. The inner diameter is a crucial dimension in this part of the feedthrough body.

The precision inserts for the MDC-II feedthroughs were machined out of extruded Delrin$^{\mathrm{TM}}$. The machining process left a small tab of material covering the inner diameter of the insert that had to be removed by hand before

Table 20: MDC-III Feedthrough specifications

Endplate thickness	4 cm
Feedthrough length	5.8 cm
Endplate hole diameter	$4.0\pm^{0.018}_{0.000}$ mm
Feedthrough diameter	$4.0\pm^{0.000}_{0.018}$ mm
Small hole length	2.0 ± 0.05 mm
Small hole diameter (sense and potential wires)	0.15 ± 0.025 mm
Small hole diameter (field wires)	0.25 ± 0.025 mm
Concentricity (small hole and outer diameter)	0.025 mm
Pin diameter	1.5 ± 0.5 mm
Total tolerance	± 0.0667 mm

the insert was placed in the feedthrough body. This laborious process will be avoided in the new feedthroughs by producing the precision inserts from synthetic sapphire. The fabrication tolerances and electrical properties for this material are better than plastic, and there will be a smaller probability of the wire deforming the insert.

4.3.3 Solder Pin Design

To hold the wires, under tension, between the endplates, requires some method of fixing the wires in the feedthroughs. We will use gold-plated solder pins. Soldering is preferred over crimping because of our experience with producing reliable solder connections. Both MDC-I and MDC-II used solder pins. The pins will occupy most of the length of the feedthrough to provide a good gas seal. The solder pins also provide a connecting point to bring high voltage into the chamber and bring signals out. There is a notch on the outer end of the pin to accomodate the solder fixing the wire to the pin. There will be no solder on the outer surface of the pin, so there will be no problems with a distorted pin shape interfering with the connectors that fit over the pins.

The pins will be fabricated out of brass (or a similar material) by drawing a tube of material down to the required dimension. After the pins are cut to length, another machining step is necessary to cut the solder knotch in one end of the pin. After a thorough cleaning, the pins will be gold plated to improve electrical conductivity and solderability.

4.3.4 Quality Assurance and Control

Based on CSU experience in producing feedthroughs for the BES MDC-II and the BaBar Main Drift Chamber, we will be using a series of quality control and assurance steps during the fabrication of the feedthroughs. These will include numerous visual inspections, high voltage tests, and mechanical and chemical tests.

The feedthroughs will be molded from virgin material. No mold release agents or lubricates will be used either during molding or in subsequent machining operations needed to remove excess plastic. Samples of the molded feedthroughs will be sent to the polymer manufacturer for inspection and testing to determine the polymerization (*e.g.* melt index testing) and crystallization (*e.g.* differential scanning calorimetry) in the molded feedthroughs. These test will help determine whether or not the material has been handled according to the manufacturer's recommendations. We will also do detailed visual inspections of the feedthroughs at CSU using scanning electron microscopy and polarized light microscopy. By examining cross-sections of a sample of feedthoughs with these instruments, we can determine if there are voids in the feedthroughs, the quality of the inner and outer surfaces, and, if applicable to the type of plastic chosen, perform a qualitative assessment of the crystallization of the plastic.

The molded feedthoughs will be handled using a protocol similar to the one developed for the BaBar feedthroughs. Feedthroughs will be molded and handled in traceable batches, with each cleaning, testing, and assembly step documented. The precision inserts will be treated in a similar fashion. Upon receipt from the molder, each batch will be visually inspected and cleaned. Each feedthrough will be fitted with a precision insert. The feedthroughs will then be placed in aluminum blocks by batches for the remaining tests. The feedthroughs will remain in the blocks until they are packaged for shipment to IHEP. Feedthroughs will be measured for concentricity using a video-optical coordinate measuring machine with a computer interface to facilitate the storage and subsequent analysis of these measurements. During this measurement any feedthrough found outside of specifications will be rejected.

Each feedthrough will be electrically tested by inserting a solder pin into the feedthrough. A voltage in excess of the planned high voltage will be applied to each solder pin while the aluminum block is held at ground potential. Initial measurements of current draw and micro-discharging will be made, after which the voltage will remain on for a period of several hours. Final current and micro-discharge measurements will be made before terminating the voltage test. Results of these tests will be traceable to individual batches. In addition, several feedthroughs from each batch will be diverted to a long-term (many months) high voltage test to look for possible polymeric degradation caused by exposure to a high electric field. Following the high voltage test, the solder pins will be removed, and the feedthroughs will be removed from the aluminum blocks for packaging and shipment to IHEP.

4.4 MDC Performance Summary

The summary of the performance we expect is:

1. Solid angle acceptance: 95% of 4π (second layer), 90% of 4π
2. Spatial resolution for single wire: $\sigma(x)$ = 180-250 μm
3. z-resolution for a single wire: $\sigma(z)$ = 3-5 mm
4. Momentum resolution:

$$\left(\frac{\sigma_{p_t}}{p_t}\right)^2 = \left(\frac{\sigma_{p_t}}{p_t}\right)^2_{\text{spatial}} + \left(\frac{\sigma_{p_t}}{p_t}\right)^2_{\text{mult.scat.}} = (0.6\%P_t)^2 + (1.2\%)^2 \quad (32)$$

5. dE/dx energy resolution: FWHM/E$_{(\text{most probable})}$ = 8.5%
6. Efficiency for a single wire: 97%

4.5 Background Calculation

Monte Carlo simulations of beam-related backgrounds have been performed for the upgraded BEPC machine in order to design improved masking for the BES detector. The main sources of beam-related backgrounds are the scattering of beam particles from residual gas inside the beam pipe and synchrotron radiation from beam particles traversing the last dipole magnet and quadrupole magnets near the IR. These backgrounds are a more serious consideration in the upgraded BEPC due to the increased beam currents, smaller beam pipe radius inside the BES detector, and mini-beta quadrupoles.

The program `DECAY TURTLE` was used with the full machine optics to simulate Coulomb scattering of beam particles from residual gas in the "vacuum" and beam-gas bremsstrahlung. The scattered electrons and photons were then used as input to `EGS4` simulations of material in the machine-detector interface region. Problems in determining absolute background rates in the BES detector include lack of precise knowledge of the residual gas pressure and composition which should be used in the `DECAY TURTLE` simulations, the simplified cylindrically symmetric geometries used in the `EGS4` simulations, and the absence of shower debris from showers beginning upstream of the region simulated by `EGS4`. However, the relative simulated background rate for the upgraded BEPC machine should be more reliable. Studies on the BEPC optics indicate that adjustable aperture masks between Q1 and Q2, where off-axis or off-energy scattered particles tend to be separated from the unscattered beam, may be able to reduce backgrounds in BES by a factor of about five.

5 Preamplifiers

Signals on the sense wires of MDC-2 are amplified by preamplifiers that are mounted directly on the endplate of the drift chamber. These devices use the NH19-6112 hybrid amplifier that was developed by NIKHEF for the L3 experiment [44]. The NH19-6112 hybrid is a single channel amplifier that converts an input current signal into an AC coupled, 50 ohm differential pair output with a gain of $2 \times 12.5\mathrm{mV}/\mu\mathrm{A}$, with an input noise level less that $0.01\mu\mathrm{A}$. In BES, these preamps are used four to a card in a configuration where cross-talk signals from neighboring sense wires are corrected by voltage dividers connected between the input lines.

For MDC layers 4 through 10, the preamplifier cards are the same as those used for the original MDC-I; additional boards, fabricated by the CSU group and mounted next to the preamps on the endplate, perform the HV decoupling function. For MDC layers 1 through 3, there is not enough room for extra HV decoupling cards, so new, miniaturized versions of the preamp cards with on-board HV decoupling capacitors were fabricated by the Hawaii group. The board space needed for the circuitry was reduced by employing surface mount components for the voltage dividers and output decoupling capacitors. These new boards used NH19-6112 hybrids that were salvaged from the layers 1-3 MDC-1 preamps.

In applications at CERN, the NH19-6112 hybrid has been superseded by a new hybrid, the FBPANIK-04, which has four channels on a single wafer, each with four times the gain of the NH19-6112 [45]. These improved hybrids are available from the METALLUX in Mendrisio, Switzerland for 17 CHF ($\sim$ \$12) per 4-channel wafer.

For MDC-III, we propose to replace all of the MDC-II front-end preamp cards with new units that incorporate the FBPANIK-04 hybrid wafer and have on-board HV decoupling capacitors. This has a number of advantages:

- The higher gain of these preamplifiers will enable us to run MDC-III with high voltages that are approximately 10% lower than those for MDC-II, which will provide for more stable operation and a longer chamber life.

- The inventory of spare NH19-6112 preamplifiers at IHEP is quite low. If we continue to use these on MDC-III, we will be vulnerable to failure of these hybrids. As part of this proposal, we include buying a sufficent number of FBPANIK-04 hybrids to provide an adequate supply of spares.

- The proposed preamps will be smaller than the existing MDC-II preamps and will preclude the need for the extra HV decoupling cards for layers 4 through 10. This will reduce the congestion in the chamber endplate region, facilitating maintenance and repair.

The proposed new preamplifier card will be functionally similar to the new layer 1 through 3 cards that the Hawaii group has prepared for MDC-II. The Hawaii group has received some sample FBPANIK-04 hybrids from the L3 group and is currently studying possible PC board layouts. In addition to making the Layer 1 through 3 preamp cards for MDC-II, the Hawaii group built all of the front end electronics for the Vertex Detector that was installed in BES as part of the BES upgrade. These electronics have performed reliably and since their installation in early 1996.

6 The BES Collaboration

BES has been a successful collaboration between Chinese and US physicists for several years. Starting with an improved tau mass measurement that incorporated more tau decay modes, the collaboration has developed the means to work cooperatively on the planning of physics runs, the reconstruction and analysis of data, and the writeup of results for publication. BES has adopted a co-spokesperson administration, where the day-to-day responsibilities of the collaboration are divided between a Chinese co-spokesperson and a US co-spokesperson. This year the collaboration has instituted co-analysis coordinators, again with one Chinese and one US.

The US collaborators meet once a month, relying heavily on ISDN video conferencing. A few of these meetings are designated corporeal meetings, where more lengthy and detailed discussions can take place. The responsibility for organizing these meetings rotates among the US member institutions. Every year at the beginning of summer there is a collaboration meeting held in China where detailed discussions of run plans and publications takes place.

Each institution has the necessary experience and expertise for their assigned tasks. UH constructed the front end electronics for the Vertex Chamber. CSU fabricated the feedthroughs for MDC-II and the BaBar Main Drift Chamber. IHEP sucessfully constructed and commissioned two large drift chambers.

The American BES groups include the University of Hawaii (professors S. Olsen and F. Harris and graduate students D. Kong, D. Paluselli, and L. Pan), the University of Texas at Dallas (professors J. Izen and X. Lou), SLAC (professor W. Dunwoodie), and Colorado State University (professor W. Toki, postdoc R. Malchow, and graduate student W. Yang). All of these institutions will continue in the collaboration during construction of the chamber and subsequent data taking and analysis.

At the University of Hawaii, faculty members Harris and Olsen will continue their involvement in the BES experiment. This will continue to be Harris' main research activity and, although Olsen's primary focus is the BELLE experiment, he expects to maintain a significant participation in BES.

Harris will continue as U.S. analysis coordinator, supervise PhD student Kong's thesis on the R measurement, and continue his analysis of $\psi(2S) \rightarrow J/\psi$ transitions. Olsen will supervise the completion of the PhD theses of

Pan and Paluselli and continue his analyses of hadronic charmonium decays.

If the MDC-III proposal is approved, the Hawaii group will supervise the fabrication of the structural components of the new drift chamber at the University of Hawaii Engineering Support Facility, as well as the design and construction of new preamplifier cards. This will be done by Olsen, with help from Harris and IHEP Director Zheng, who expects to be on sabbatical leave at the University of Hawaii during the latter half of 1998. (Partial support for Zheng's visit will be provided by the University of Hawaii.)

Olsen and Harris will continue in BES and participate in the analysis of the data taken with the new MDC. As many as two Hawaii students will be supported to work on BES if they are available.

At Colorado State University, Malchow and Toki will continue their involvement with the BES experiment. Malchow's main activity will be the BES experiment. Malchow is the US co-spokesperson for the collaboration and averall project manager of the MDC-III proposal. Toki is on leave of absence working at SLAC full time as Babar Analysis Physics coordinator, but after his term finishes in August 1998, he can participate in BES efforts, where he expect to contribute an important fraction of his research time. Toki continues to direct the research of his graduate student, Yang, on analysis of neutral ψ' decays to radiative states. A new graduate student from IHEP, J. Zhang, is arriving at CSU, and he may participate in BES research.

If the MDC-III proposal is approved, the Colorado State group will fabricate the feedthrough components. Malchow will be the project manager of the feedthrough efforts at Colorado State and D. Warner, the engineer who supervised the Babar feedthrough project that produced +100K feedthroughs, will supervise the BES feedthrough project. This project will utilize undergraduates and technicians, some of whom are experienced with the Babar feedthrough project. Some of the existing tooling may be used as prototypes to develop BES feedthrough prototypes.

Toki and Malchow will continue in BES and participate in the analysis of the data taken with the new MDC. If funds permit, we will get graduate student(s) involved with the high statistics BES physics on J/ψ, $\psi(2S)$, or $\psi(3770)$ data which will provide ample new physics opportunities for a PhD thesis.

7 Schedule

Construction of the new drift chamber will begin as soon as the grant is awarded. An outline of our proposed schedule is shown in Table 21. It will take three months to procure the endplate material and seven months to machine them; it will take eight months to begin shipping feedthroughs to IHEP, and another three months to complete feedthrough production; it will take seven months to produce the outer cylinder; and it will take eight months to string and install the chamber. We plan on installing the new drift chamber in summer 1999.

Table 21: Proposed schedule for the construction of MDC-III.

1998	1 January	Start endplates and outer cylinder at UH
		Start feedthroughs at CSU
	1 September	Begin delivering feedthroughs to IHEP
	15 October	Endplates and outer cylinder delivered to IHEP
		Begin stringing chamber at IHEP
	1 December	Finish delivering feedthroughs to IHEP
1999	1 July	Installation of chamber in BES
	1 October	BES startup

8 Budget Discussion

The costs of producing new feedthroughs and solder pins has been estimated by CSU, and are detailed in Table 22 (attached to the end of this proposal). These include material and fabrication, assembly labor at CSU, engineering, and shipping the feedthroughs and pins to IHEP. Based on our experience in producing feedthroughs for MDC-II and BaBar, a 30% overproduction is reasonable for samples, testing, failures, restringing bad wires, and construction of test/monitor chambers.

Travel from CSU to IHEP and UH is necessary for project management and engineering consultation. The number of trips budgeted is based on our recent experience.

The costs of the new endplates and outer cylinder have been estimated by UH. These include material, fabrication, and shipping of the completed parts to IHEP. The total estimated cost for these components is \$261,600. These estimates are summarized in Table 23 (attached to the end of this proposal).

Our estimated cost for new preamp boards is based on actual costs for the layer 1 through 3 cards plus a quote from METALLUX for the 4 channel FBPANIK-04 hybrids. The total cost estimate for the preamps is \$72,000. Details of this estimate are given in Table 23 (attached to the end of this proposal).

A summary of the total cost of this project is shown in Table 24 (attached to the end of this proposal).

9 Summary

We propose to build a new Main Drift Chamber (MDC-III) for the BES experiment. The present drift chamber (MDC-II) is failing because of premature aging of its feedthroughs. The endplates, outer cylinder, and frontend electronics will be built by UH. The feedthroughs will be built by CSU. Assembly and stringing of the chamber will be done by IHEP. The new drift chamber will maintain the ability of BES to make high precision measurements in the tau/charm sector. The total amount requested for the US portion of this project is \$624,375.

References

[1] N. Cabibbo and R. Gatto, Phys. Rev. **124**, 1577 (1961).

[2] S. Eidelman and F. Jegerlehner, preprint PSI-PR95-1, January 1995.

[3] M. Swartz, SLAC-PUB-95-7001 (1995).

[4] A. Martin and D. Zeppenfeld, Phys. Lett. B345, 558(1995).

[5] H. Burkhardt and B. Pietrzyk, Phys. Lett., B356,398 (1995).

[6] B. Pietrzyk, Acta Physica Polonica, B28, 673 (1997).

[7] M. Peskin, private communication.

[8] M. Peskin and T. Takeuchi, Phys. Rev, D46, 381 (1992), see eqns. 3.8, 3.13, 4.3 and 4.4.

[9] For a summary using Summer 19 97 results, see W. Hollik, "Review: Status of the Standard Model", hep-ph/9711492, Nov. 27, 1997 and for an update of the Particle Data Tables see P. Langacker and J. Erler, "Unification or Compositeness", hep-ph/9703438, July 19, 1997.

[10] R.M. Barnett et al. (Particle Data Group), Phys. Rev. **D54**, 1 (1996).

[11] B.L. Roberts, Status of the Theoretical Value of $(g-2)$, (1996).

[12] J. Adler et.al., Phys.Rev.Lett.,60,89(1988) and J. Adler et.al., Phys. Rev.Lett., 64,169(1990).

[13] J. Bai et. al., Phys.Rev.Lett., 74, 4599 (1995).

[14] CLEO group, Phys.Rev.Lett., 71,3070(1993), Phys.Rev.Lett., 72, 2328(1994), Phys.Lett. B378,364(1996), Phys.Lett. B324, 255(1994).

[15] For an early reference see D. Robson, Nucl.Phys.B130:328,1977.

[16] For a discussion of the IBM and UKQCD results see T. DeGrand, SLAC Summer School Lectures, August 1996.

[17] UKQCD group, Phys. Lett. B309, 378 (1993); Sexton, Vaccarino, Weingarten, Phys. Rev. Letts, 75, 4563 (1995).

[18] For MIT bag models see T. Barnes, Caltech Thesis, 1977; for constituent gluon models see D. Horn and J. Mandula, Phys. Rev D17, 898 (78); for MIT bag models see T. Barnes. F.E. Close, F. de Viron, Nucl. Phys. B224, 241 (1983).

[19] See reviews by W. Toki, "Search for Glueballs", SLAC Summer School Lectures, August 1996; For pedogical introduction see F. Close, AN Introduction to Quarks and Partons, Academic Press 1979); For a summary of J/ψ results from Mark III and DM2, see L. Kopke and N. Wermes, Physics Reports, 174, 67 (1989).

[20] Gilles Forconi, "First Indication for the x(2230) Production in Hadronic Z decays", Hadron 97 Conference, BNL, August 1997.

[21] Andrew Kirk, "Search for non-$q\overline{q}$ mesons in the WA102 Experiment at the CERN Omega Spectrometer", Hadron 97 Conference, August 1997.

[22] L. P. Chen, Phd Thesis, Vanderbilt University and for a more recent discussion see W. Toki, SLAC Summer School Lectures, "Search for Glueballs", August 1996. and SLAC-PUB-5669.

[23] C. Strassburger, "Scalar Glueball and 3P0 Mesons", Hadron 97 Conference, BNL, August 1997.

[24] D. Bugg et al., Phys. Lett. B353,378(1995).

[25] W. Toki, "Search for Glueballs", SLAC Summer School Lectures, August 1996

[26] D. Thomspon et al., Phys.Rev.Lett.79:1630,1997.

[27] C. Edwards *et al.* (Crystal Ball collaboration), Phys. Rev. Lett. **48**, 70 (1982).

[28] W. Buchmüller and S-H.H. Tye, Phys. Rev. **D24**, 132 (1981).

[29] V. Vasilis and N. Byers, Phys. Rev. **D28**, 2908 (1983).

[30] S.F. Tuan, K.T. Chao and Y.F. Gu, *On trigluonia in charmonium physics*,UH-511-790-94 (revised), submitted to Phys. Rev. **D**.

[31] V.A. Novikov and M.A. Shifman, Z. Phys. **C8**, 43 (1981).

[32] B.L. Ioffe and M.A. Shifman, Phys. Lett. **B95**, 99 (1980).

[33] M. Oreglia *et al.* (Crystal Ball collaboration), Phys. Rev. Lett. **45**, 959 (1980); T. Himel *et al.* (Mark-I Collaboration), Phys. Rev. Lett. **45**, 920 (1980).

[34] Y.F. Gu *Results on hadronic $\psi(2S)$ decays into VP and VT final states*, contributed paper to the Minneapolis DPF meeting, August 1996.

[35] L.J. Pan *$\psi(2S)$ decays to baryon-antibaryon pairs*, ibid.

[36] M.E.B. Franklin *et al.* (Mark II Collaboration), Phys. Rev. Lett. **51**, 963 (1983).

[37] M. Chaihian and N.A. Törnqvist, Nucl. Phys. **B323**, 75 (1989).

[38] Stephen S. Pinsky, Phys. Lett. **B236**, 479 (1990).

[39] S.J. Brodsky, G.P. LePage, and S.F. Tuan, Phys. Rev. Lett. **59**, 59 (1987).

[40] W-S. Hou, and A. Soni, Phys. Rev. Lett. **50**, 569 (1983).

[41] J.Z. Bai *et al.* (BES Collaboration), Phys. Rev. **D54**, 1221 (1996).

[42] W-S. Hou, Phys. Rev. **D55**, 6952 (1997).

[43] Polymeric Materials Encyclopedia, CRC Press, 1783 (1996).

[44] P. Rewiersma, *The L3 Wire-Amplifier*, NIKHEF (1986).

[45] P. Rewiersma, *FMUON-AMP (drawing)*, NIKHEF (1991); H.P. von Gunten, ETH-Zurich, private communication (1997).

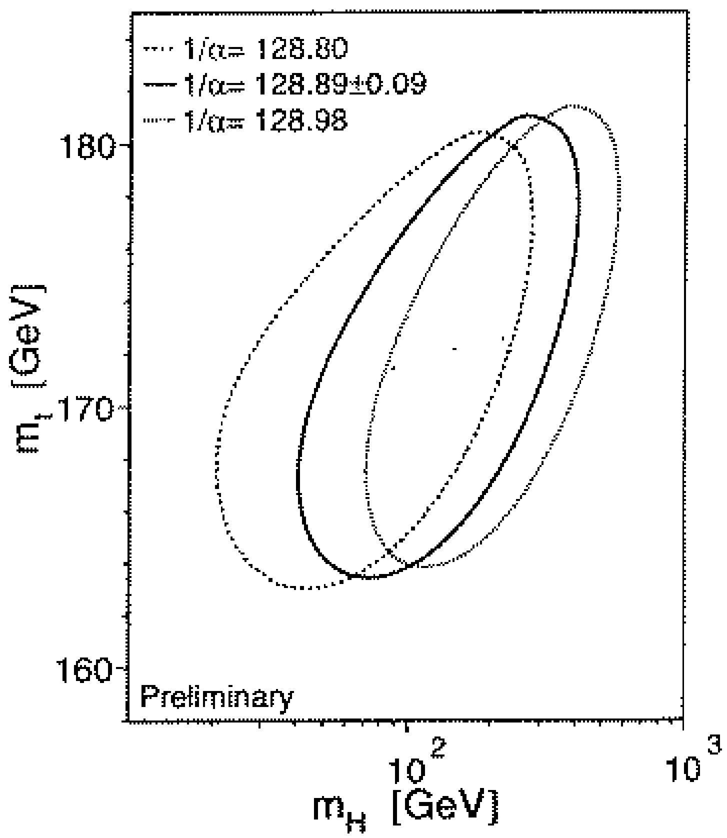

Figure 1: Estimate of M_{top} and M_{Higgs} for a given value of $\alpha^{-1}(M_Z^2)$. the upper limit for M_{Higgs} moves up by about 100 GeV if $\alpha^{-1}(M_Z^2)$ shifts upward by 0.09. (From ref. [6].)

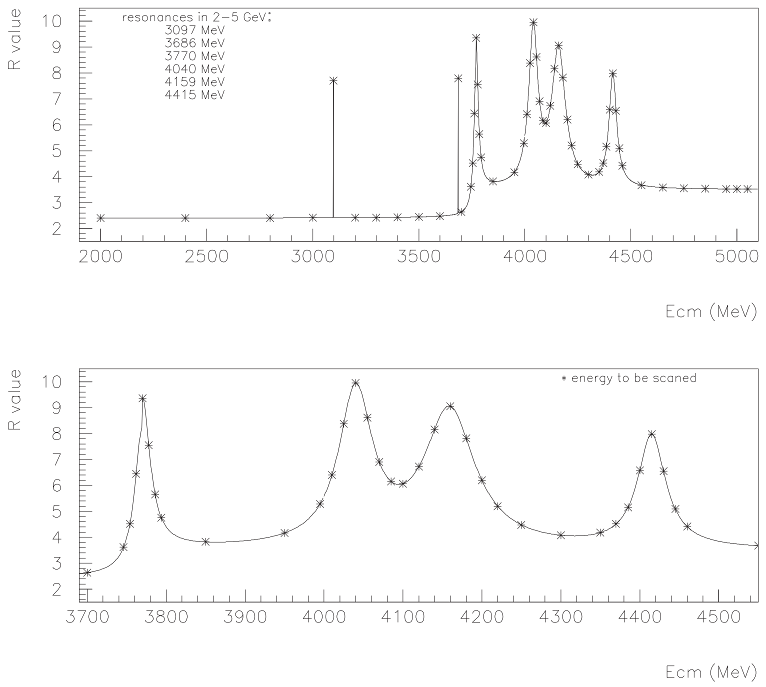

Figure 2: Proposed center of mass energy points for the R scan. At least seven points on each wide resonance will be needed to determine the peak shapes. The J/ψ and $\psi(2S)$ resonances will be used for energy calibration.

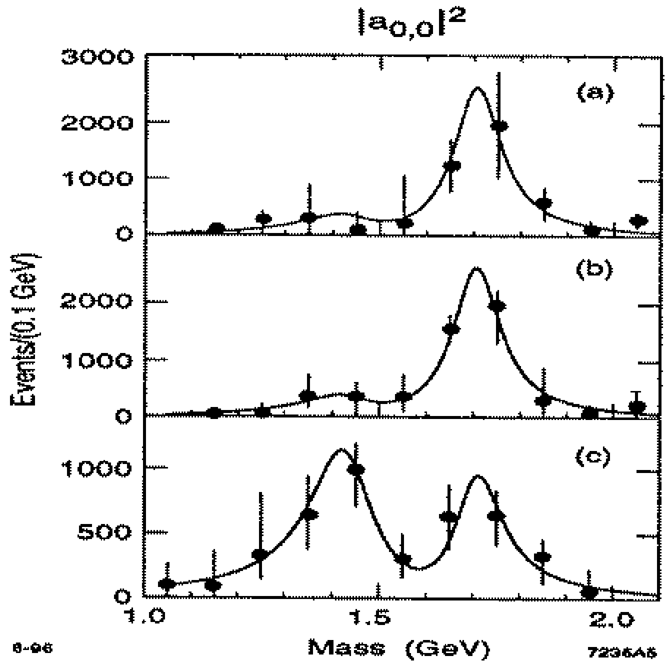

Figure 3: Mark III evidence for $f_J(1700)$. (From ref. [22].)

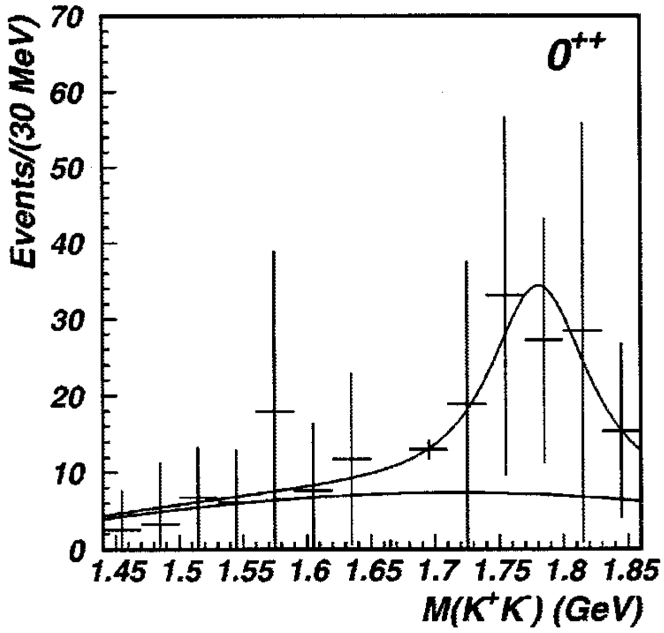

Figure 4: BES evidence for $f_J(1700)$.

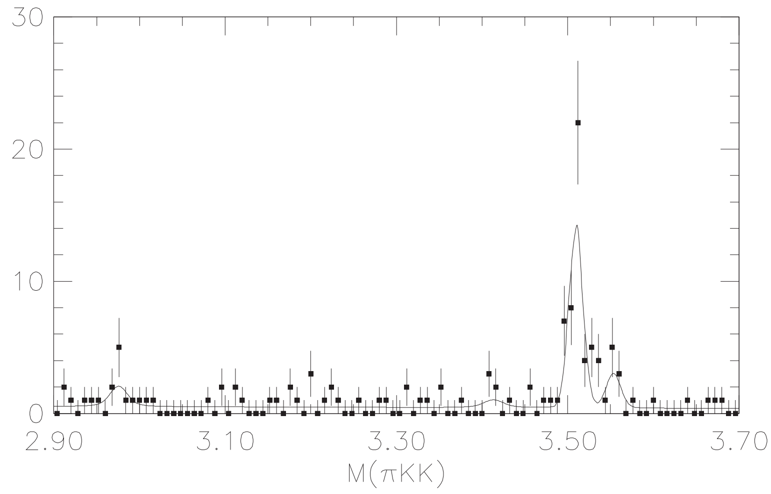

Figure 5: The $KK\pi$ invariant mass distribution from the 3.6M $\psi(2S)$ event sample. The superimposed curve is descibed in the text.

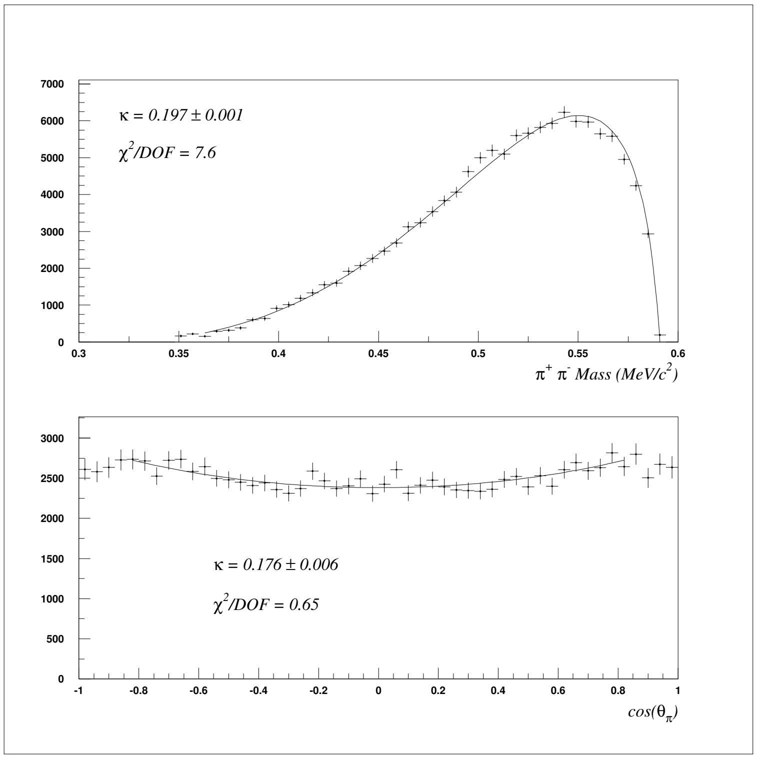

Figure 6: The top distribution is the $M_{\pi\pi}$ distribution from $\psi(2S) \rightarrow \pi^+\pi^- J/\psi$ decays. The bottom distribution is the $\cos\theta_\pi$ distribution, where θ_π is defined in the text. The points are the data corrected for efficiency, and the curve is the fit result. The fit region for the $\cos\theta_\pi$ distribution is from -0.8 to 0.8.

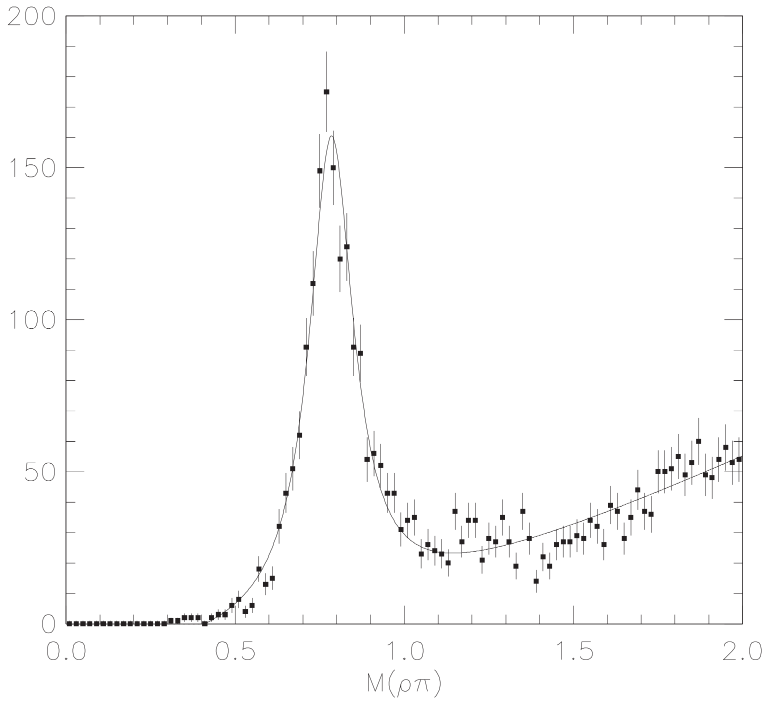

Figure 7: The $\pi\pi$ mass distribution from tagged $J/\psi \rightarrow \pi^+\pi^-\pi^0$ decays. The curve is a fit to a ρ with 1715 ± 54 events and a smooth background function.

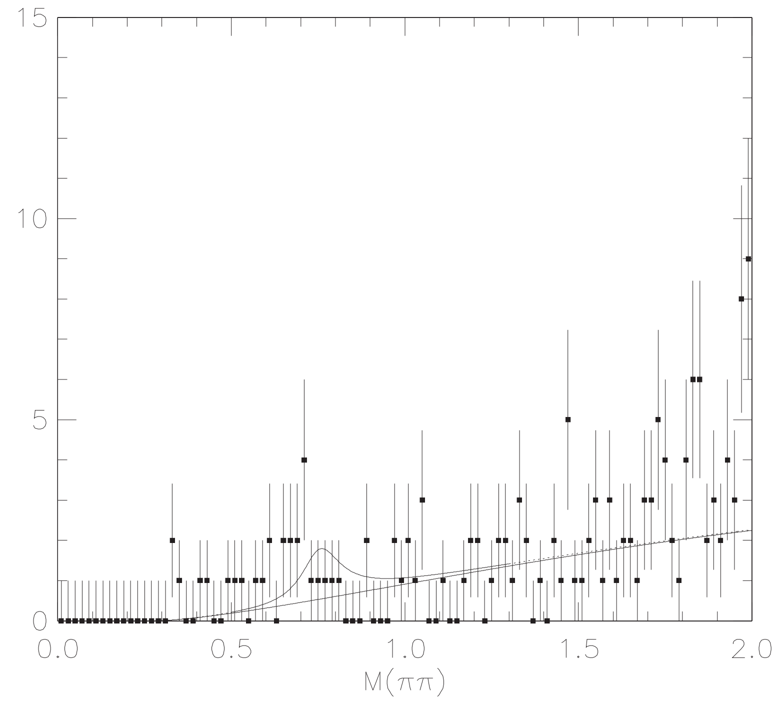

Figure 8: $\psi(2S) \to \pi^+\pi^-\pi^0$ decays. The curve is a fit to a ρ with 13 ± 6 events and a smooth background function. This is in sharp contrast with the 15%-rule expectation of a similar number of ρ events as in the tagged J/ψ sample, shown in Fig. 7 above.

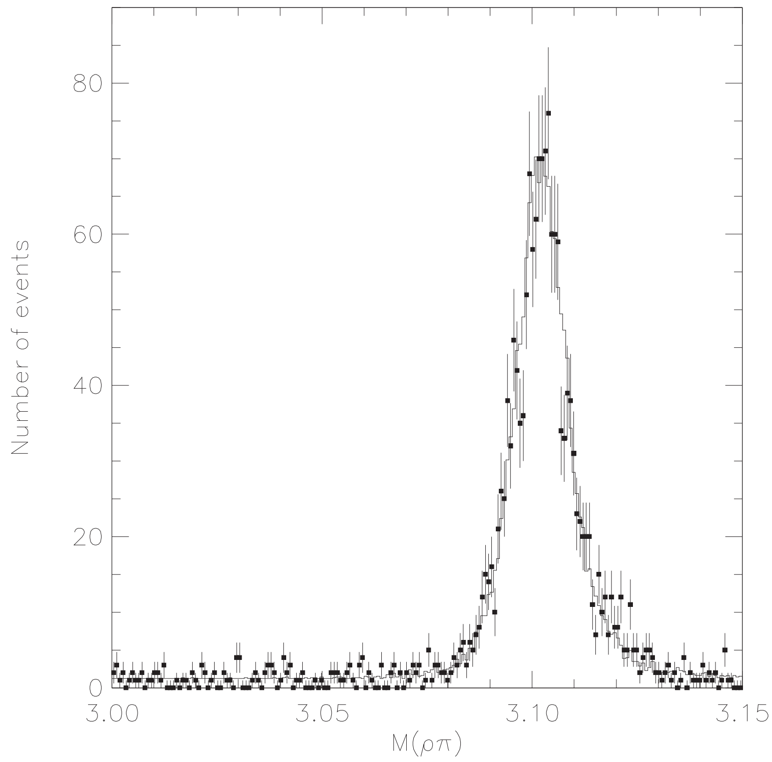

Figure 9: The $\pi^+\pi^-$ recoil mass distribution from $\psi(2S) \to \pi^+\pi^-\rho\pi$ decays. The curve is the scaled $\pi^+\pi^-$ recoil mass distribution from $\psi(2S) \to \pi^+\pi^-\mu^-\mu^+$ decays plus a constant background.

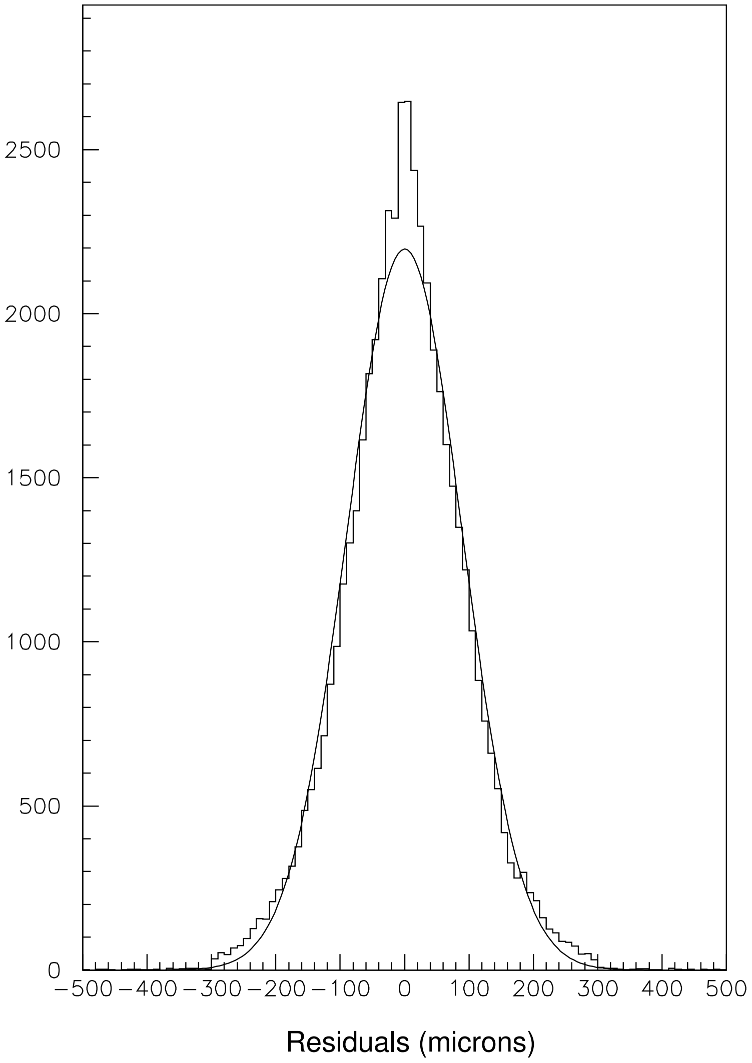

Figure 10: Residuals from Bhabha events in the Vertex Chamber. The distribution has a σ of 90 μm.

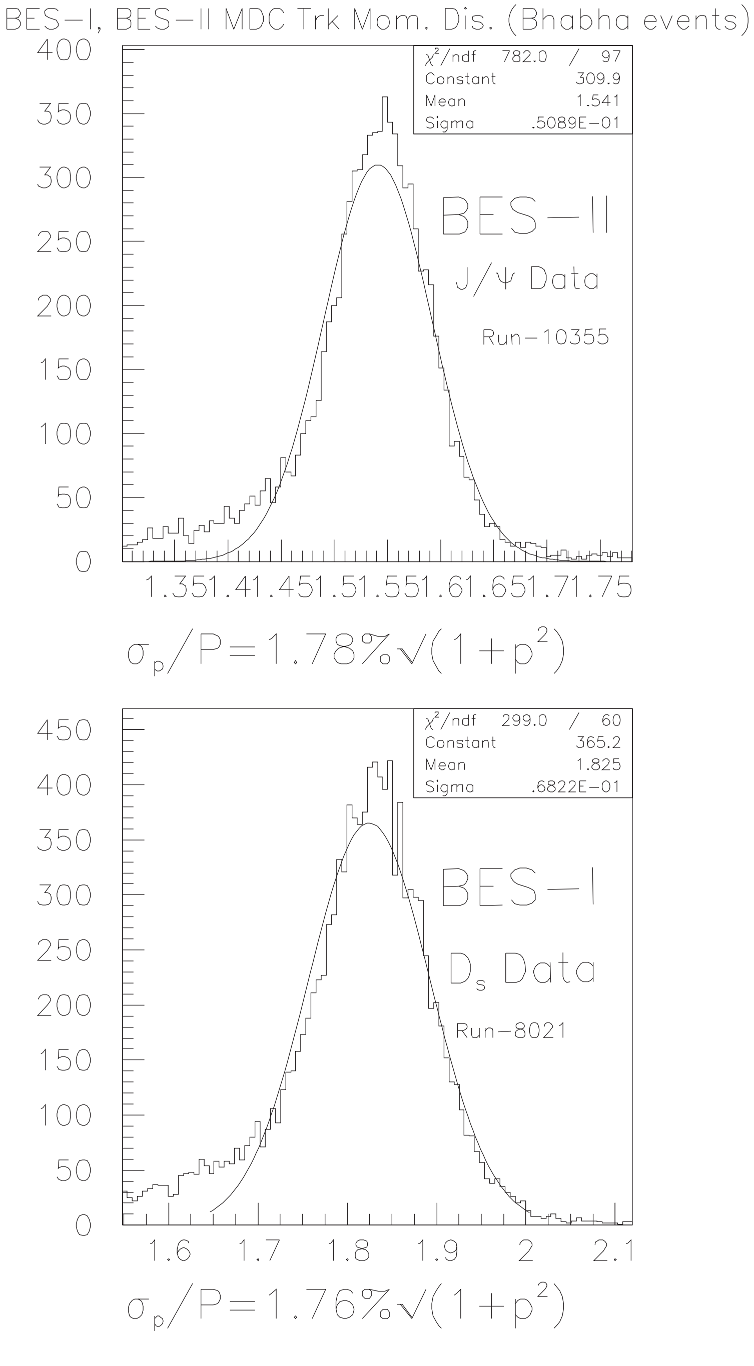

Figure 11: Track momentum distributions from Bhabha events in BES-II (top) and BES-I (bottom).

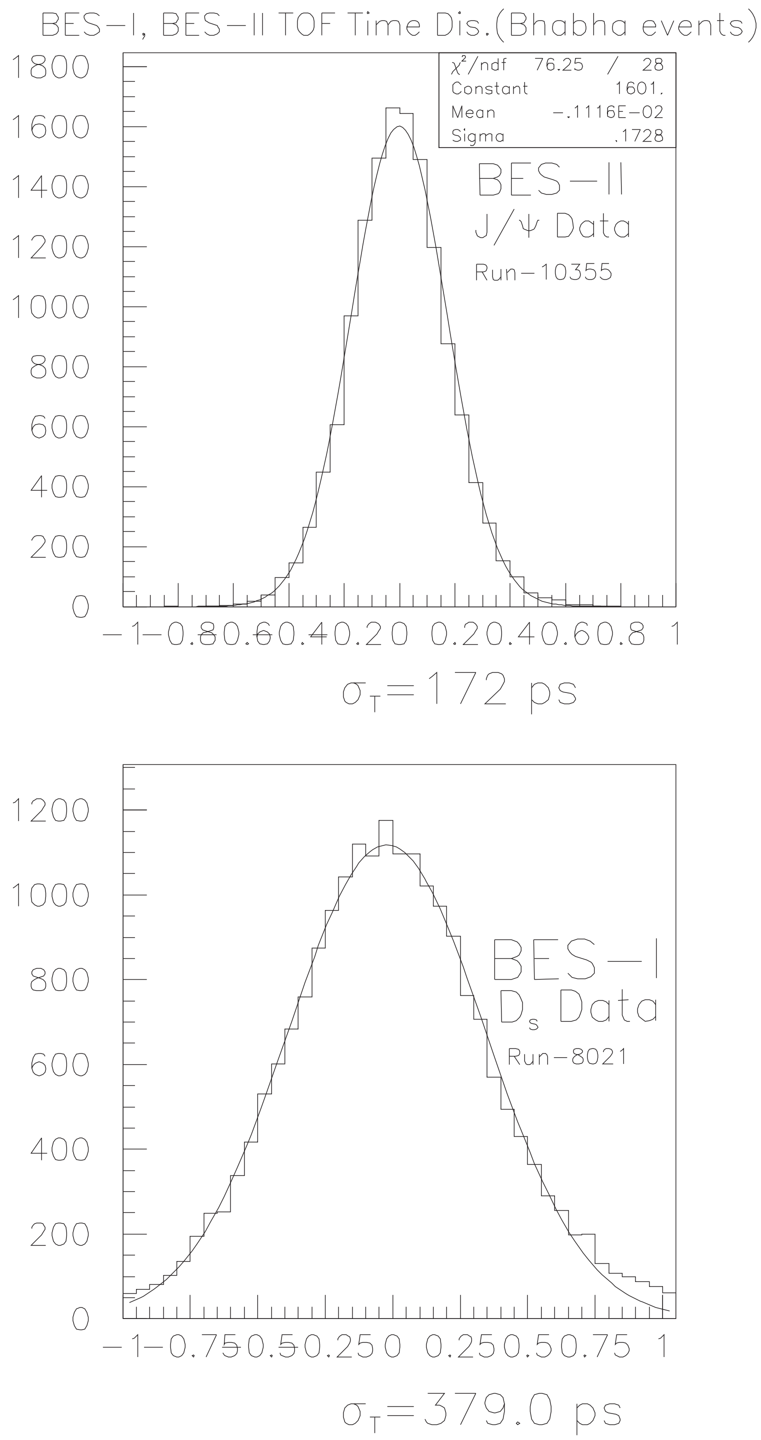

Figure 12: Time of flight timing distributions from Bhabha events in BES-II (top) and BES-I (bottom).

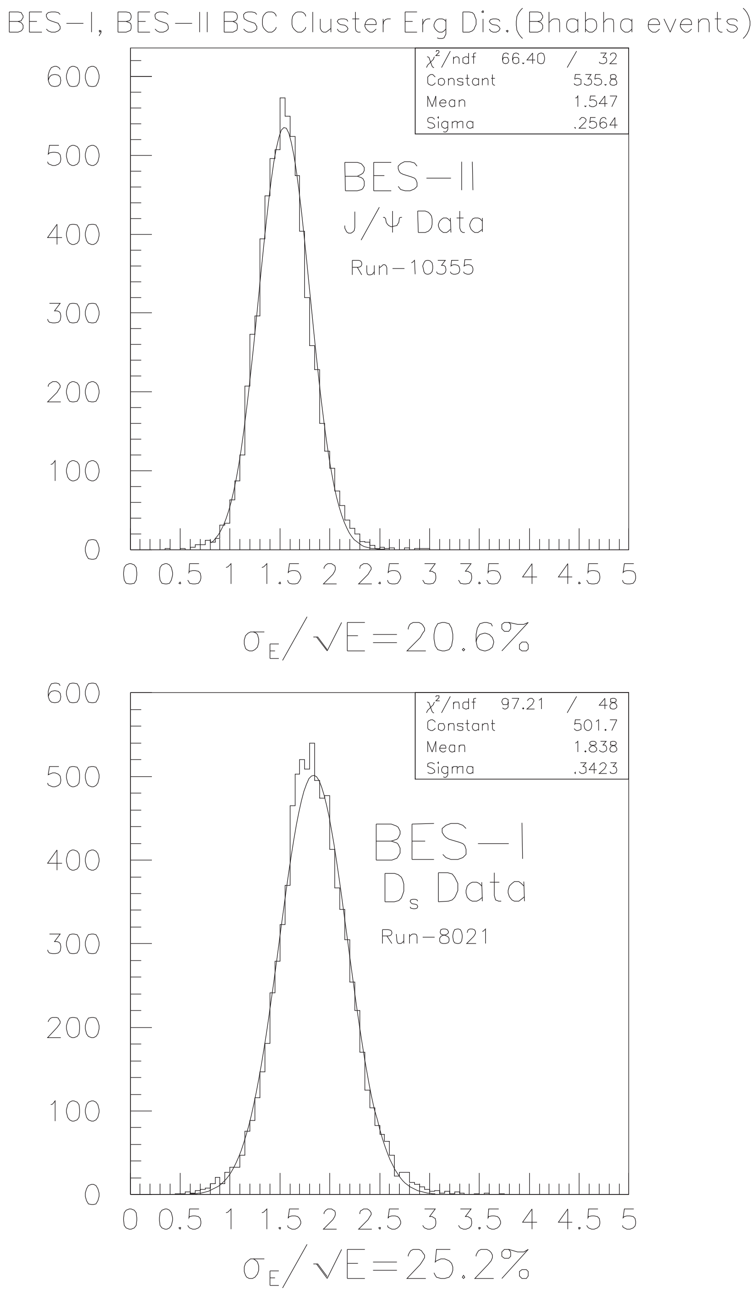

Figure 13: Energy distributions in the Barrel Shower Counter from Bhabha events in BES-II (top) and BES-I (bottom).

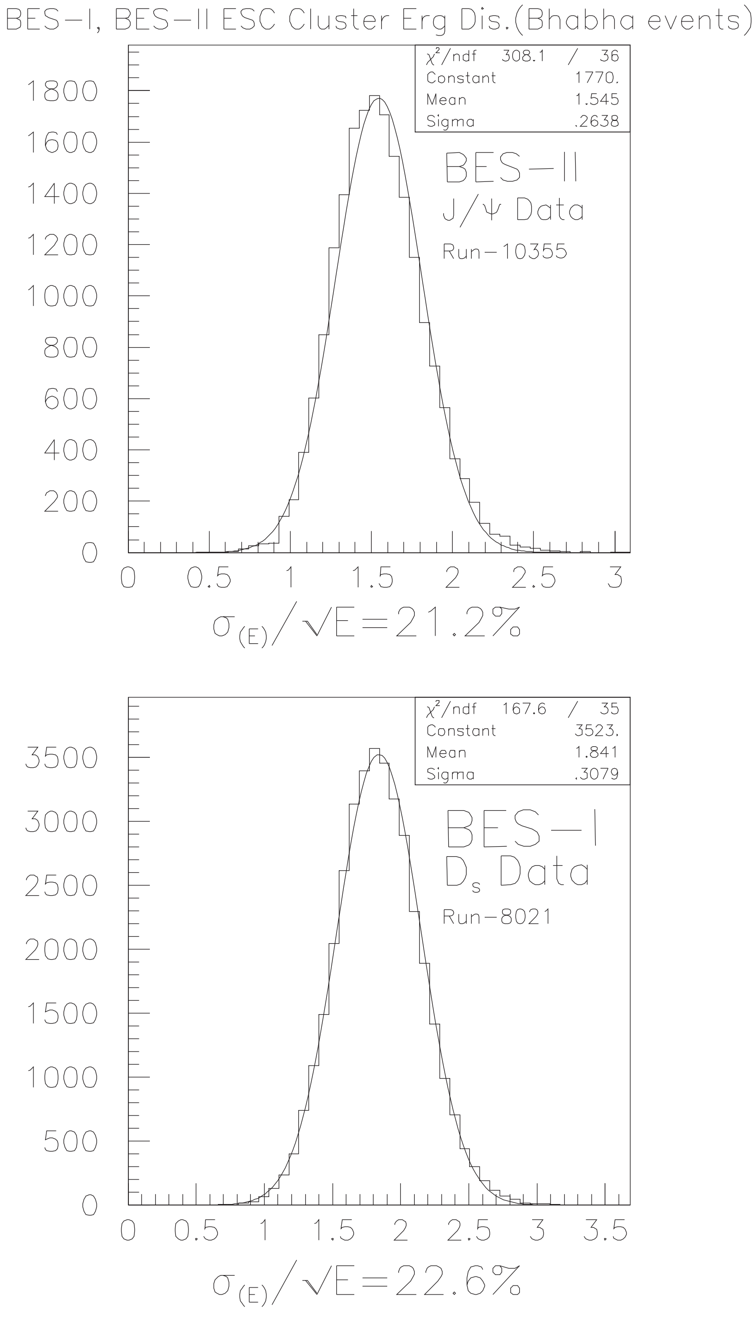

Figure 14: Energy distributions in the Endcap Shower Counter from Bhabha events in BES-II (top) and BES-I (bottom).

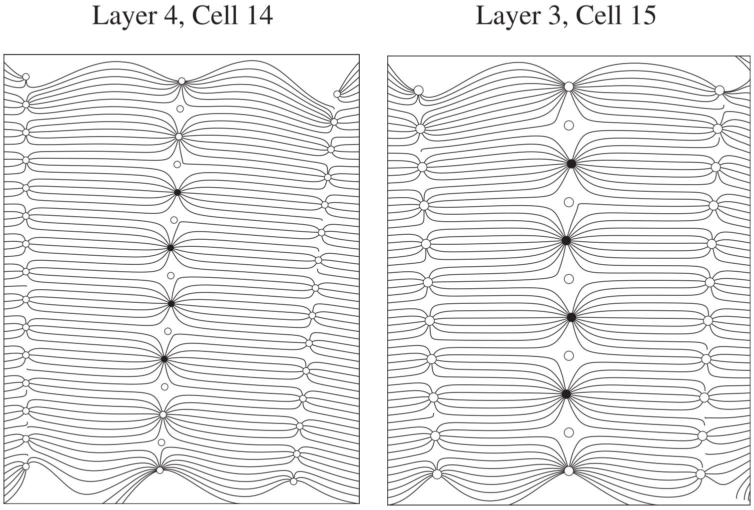

Figure 15: Calculated field lines in the Main Drift Chamber using split voltages. The sense wires are marked with filled circles. The field is nearly identical to that obtained with the field wires at +4 kV and the sense wires at ground potential.

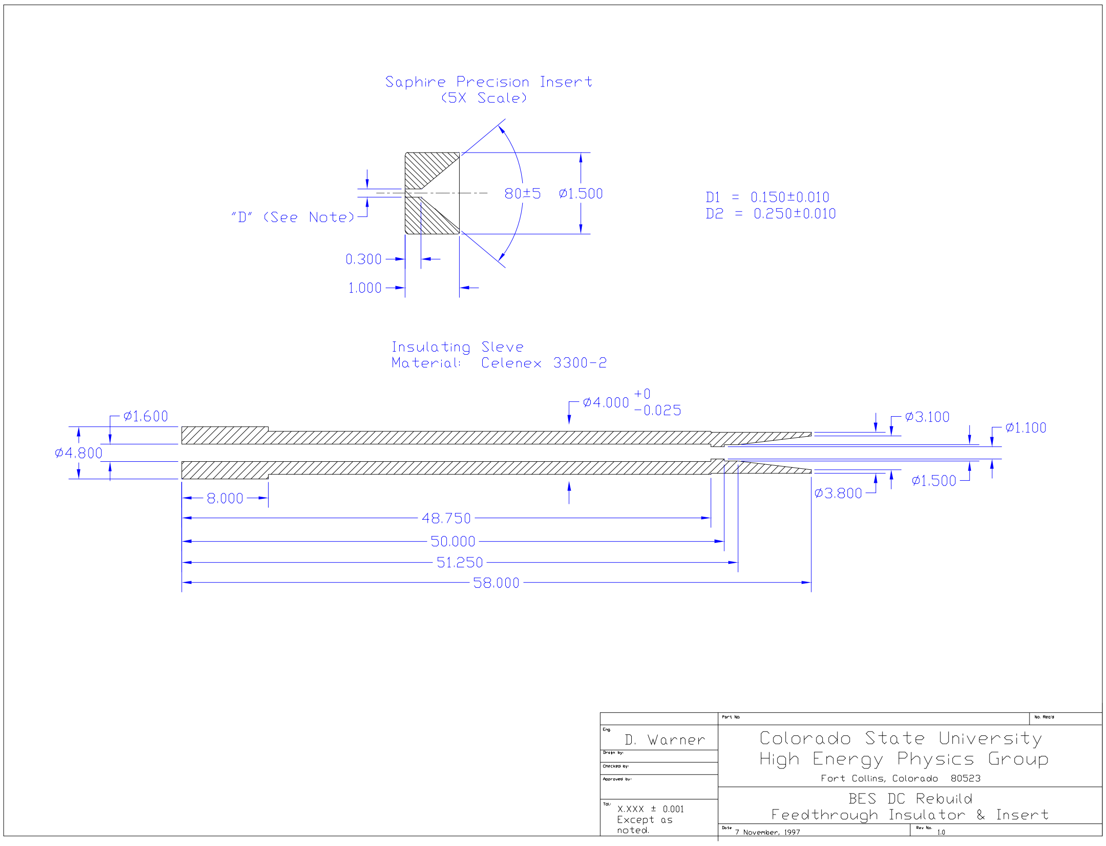

Figure 16: Design of the proposed MDC-III feedthrough. The wire is positioned by the synthetic sapphire insert.

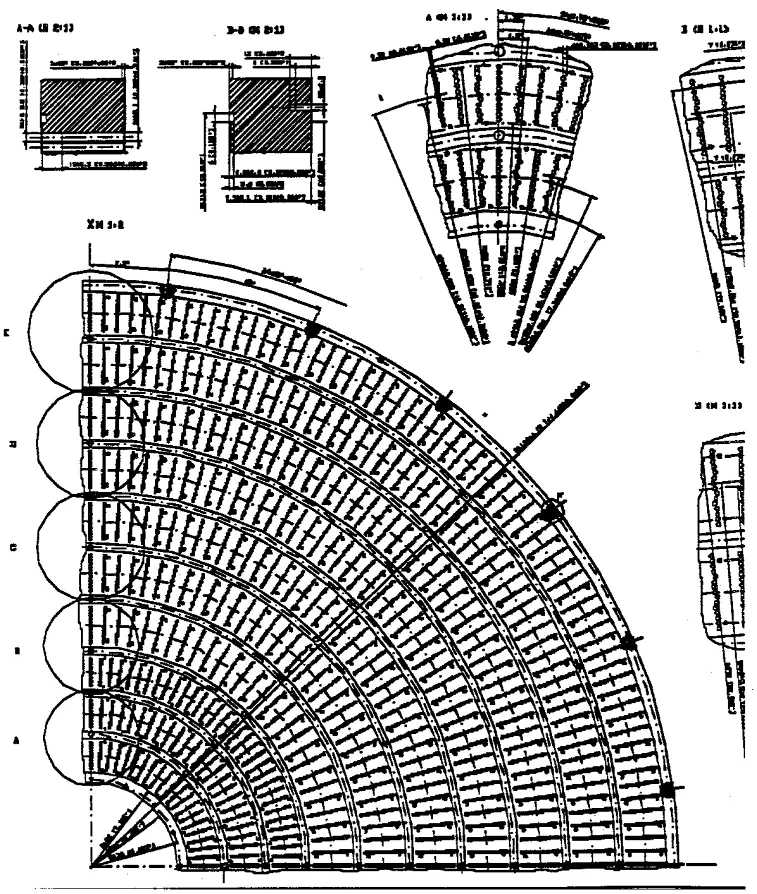

Figure 17: Sketch of one quadrant of the Main Drift Chamber.

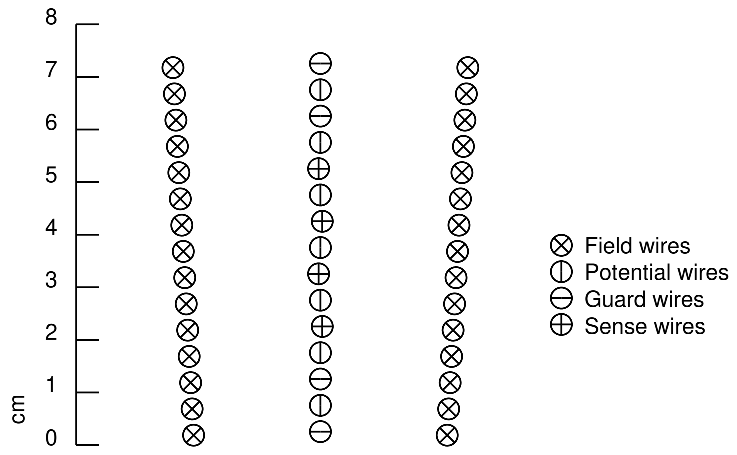

Figure 18: Sketch of a Main Drift Chamber drift cell.

Figure 19: An example of a large complex construction project successfully completed at ESF.

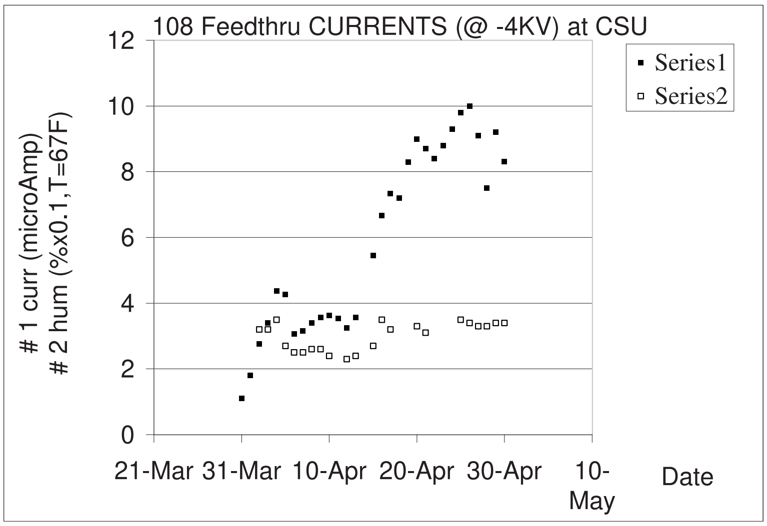

Figure 20: MDC-II feedthrough current test at CSU. The filled squares are the total current draw for 108 feedthroughs, and the open squares are the relative humidity.

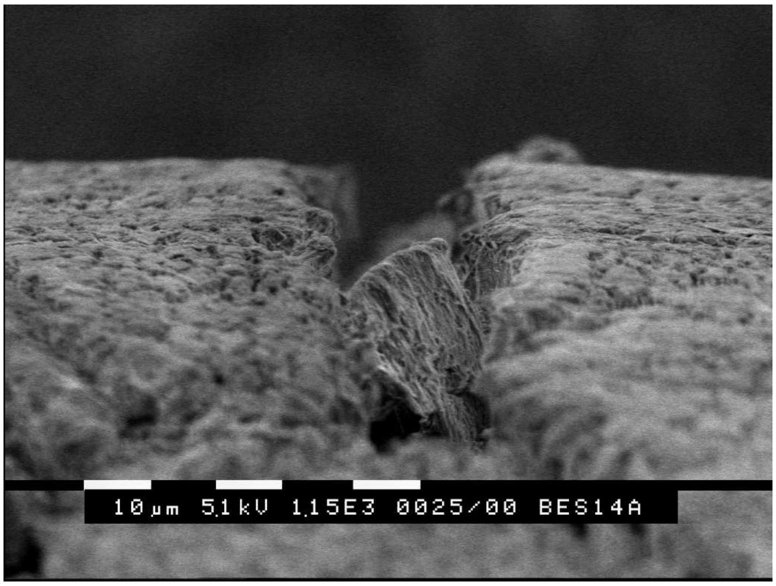

Figure 21: Large crack on a used MDC-II feedthrough. The first white section of the horizontal scale bar is 10 μm long. This micrograph was taken on the outer surface of a feedthrough that was in a prototype endplate with -4 kV applied to the solder pin.

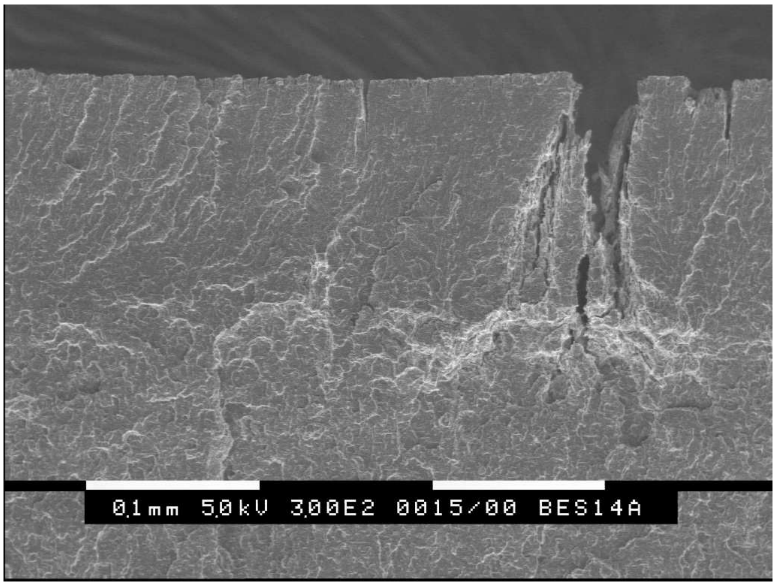

Figure 22: Cross section of a deep crack in a used MDC-II feedthrough. The puter surface of the feedthrough is visable near the top of the micrograph. The white scale bar is 100 μm long. The crack on the right has propagated deeply into the feedthrough, probably as a result of repeated micro-discharging.

Table 22: Colorado State University budget for MDC-III feedthrough and solder pin production. These costs are based on the production of 46,000 + 30% (60,000) feedthroughs and pins.

Materials			
Mold		$ 8,000	
Feedthrough bodies	0.35/ea	21,000	
Solder pins	0.783/ea	47,000	
Precision inserts	1.04/ea	62,400	
Testing fixtures		2,500	
Supplies (alcohol, gloves, etc.)		2,500	
Materials subtotal			$ 143,400
Assembly labor			
Precision inserts	0.07/ea	4,200	
Solder pins	0.14/ea	8,400	
Inspection	0.21/ea	12,600	
HV testing	0.21/ea	12,600	
Cleaning/packing	0.07/ea	4,200	
Assembly labor subtotal			42,000
EDI&A			
Engineering & supervision	10 personmonths	65,000	
Phone, video (ISDN)		5,000	
Travel to IHEP	4 trips	12,000	
Travel to UH	2 trips	3,000	
EDI&A subtotal			85,000
Shipping			
Shipping		5,000	
Customs charges		12,000	
Shipping subtotal			17,000
Total Direct Costs			**$ 287,400**
Indirect Costs			
45%, Base = $7,500 (project management travel)			3,375
Colorado State University total			**$ 290,775**

Table 23: University of Hawaii Budget for endplates, outer cylinder, and 1200 new 4-channel preamp boards

Endplates and outer cylinder			
Endplate material		$ 26,000	
Endplate milling		133,800	
Outer cylinder		89,800	
Shipping		12,000	
Endplate and outer cyl. subtotal			$ 261,600
Preamplifiers			
Engineering (100 hr)		7,200	
PCB fabrication	12.00/ea	14,400	
Parts	30.00/ea	36,000	
Assembly	12.00/ea	14,400	
Preamplifier subtotal			72,000
University of Hawaii total			**$ 333,600**

Table 24: MDC-III budget summary, combining UH and CSU requests.

Endplates and outer cylinder		
Endplate material	$ 26,000	
Endplate milling	133,800	
Outer cylinder	89,800	
Shipping	12,000	
Endplate and outer cylinder subtotal		$ 261,600
Preamplifiers		
		72,000
Feedthroughs and solder pins		
Material	143,400	
Assembly labor	42,000	
EDI&A	85,000	
Shipping	17,000	
Feedthroughs and solder pins subtotal		287,400
Total Direct Costs		**$ 621,000**
Indirect costs		3,375
Total cost of project		**$ 624,375**